J. Fluid Mech. (2022), *vol*. 943, A37, doi:10.1017/jfm.2022.428

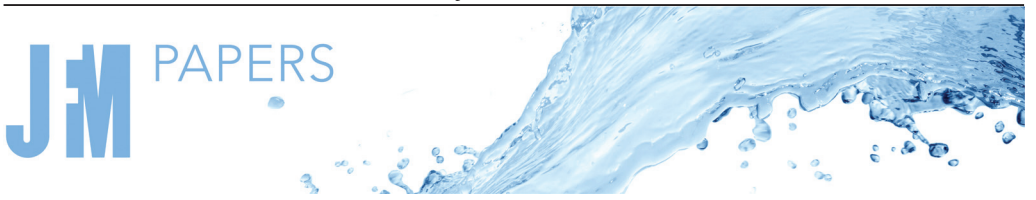

Three-dimensional flow field measurements in the wake of a tethered sphere crossing the onset of vortex induced vibrations

D. Kovalev[1], **L. Eshbal**[1] **and R. van Hout**[1],†

[1]Faculty of Mechanical Engineering, Technion - Israel Institute of Technology, Technion city, Haifa 32000, Israel

(Received 17 October 2021; revised 2 May 2022; accepted 2 May 2022)

The changing three-dimensional vortex shedding topology of a heavy, tethered sphere exposed to uniform flow crossing the onset of vortex induced vibrations (VIV) is reported together with simultaneously tracked sphere positions. Transient upstream flow conditions were imposed by increasing the reduced velocity from $U^* = 2.2$ to 4.5 ('lock-in', mode I). Three-dimensional vortex shedding under these transient conditions strongly resembled those at steady conditions at the same U^*. Changes in the wake accompanying the onset of VIV indicated several well-defined stages associated with the changing instantaneous location of the velocity deficit centroid and the wake's symmetry plane's orientation. Before the onset of VIV, the appearance of induced vortices led to lock-in of streamwise sphere oscillations prior to lock-in in the transverse direction. Shortly after ($U^* \approx 3.6$), preferential vortex shedding (wake symmetry plane aligned with tether) was lost. Upon reaching $U^* = 4.5$, flow–structure interaction reorganised vortex shedding and sphere motion, resulting in steady state conditions after some delay. At this stage, the symmetry plane was aligned perpendicular to the tether and pairs of alternately shed, single hairpins exerted transverse forcing on the sphere. At $U^* = 7.2$ (mode II, steady upstream flow), pairs of double hairpins were shed per oscillation period with maximum instantaneous vortex force coefficients that were higher than at $U^* = 4.5$. While the present Reynolds numbers (Re) were chosen low, the different identified stages in the onset of VIV are also expected to be relevant at a higher Re range.

Key words: flow-structure interactions, wakes, vortex shedding

1. Introduction

Vortex induced vibrations (VIV) are a common phenomenon when structures are immersed in flowing media. Implications may be destructive for pipelines in ocean

† Email address for correspondence: rene@technion.ac.il

engineering applications or electricity power lines in the atmospheric boundary layer (Blevins 1977; Naudascher & Rockwell 2012). Alternatively, VIV may be harnessed for green energy applications (Bernitsas *et al.* 2008). In recent decades, VIV of bluff bodies such as cylinders and spheres have been studied extensively. However, compared with VIV of elastically mounted cylinders (Bearman 1984; Williamson & Govardhan 2004), relatively little work has been done on tethered spheres. Moreover, most published research has focused on sphere dynamics and relatively little is known about the details of the three-dimensional (3-D) flow field. The latter information is essential to improve our understanding of VIV which is characterised by intricate coupling between structural and flow dynamics.

Since VIV are preceded by stationary structural conditions, it is of interest to first review the wake flow behind stationary spheres immersed in uniform flow. In this case, the governing non-dimensional parameter is the Reynolds number, $Re = U_\infty D/\nu$, where U_∞ denotes the characteristic fluid velocity at the sphere position, D denotes the sphere diameter and ν the kinematic fluid viscosity. The study of the flow in the wake of spheres has a long history. In early days, most efforts were focused on measuring the drag force exerted on a sphere exposed to a uniform flow at high Reynolds numbers (e.g. Möller 1938; Achenbach 1974). However, due to the inherent three-dimensionality of the flow and technological limitations, the exact details of vortex shedding in the wake of the sphere remained a subject of discussion. Until approximately two decades ago, the only instantaneous information on the 3-D flow structure in the wake of a sphere was based on dye or smoke visualisations (e.g. Magarvey & Bishop 1961; Leweke *et al.* 1999). The emerging picture from these studies was that, beyond the critical Reynolds number for unsteady vortex shedding ($Re \approx 270$), a train of interconnected, one-sided hairpin vortices was shed. As Re was increased, these large-scale vortices became increasingly fragmented and beyond $Re \approx 800$, the vortex shedding frequency bifurcated into two branches (Sakamoto & Haniu 1990); a low frequency branch associated with the large-scale structures and a high frequency branch associated with the small-scale structures that were the result of shear layer instabilities. The paradigm of a shed sequence of one-sided hairpin vortices was questioned by the direct numerical simulations (DNS) performed by Johnson & Patel (1999). Their simulations showed that, in contrast to the visualisations, so-called 'induced' hairpin vortices were shed in addition to the train of primary hairpin vortices observed in the visualisations. These induced vortices were periodically generated with their 'heads' pointing in the opposite direction from those of the shed primary hairpin vortices. The appearance of these induced vortices has only recently been experimentally validated by Eshbal *et al.* (2019*b*), who showed that they were the result of a rearrangement of generated vorticity by the action of the primary vortices.

The first exploratory results that showed that, much like elastically mounted cylinders (Bearman 1984; Sarpkaya 2004; Williamson & Govardhan 2004), tethered spheres also undergo VIV, were published by Govardhan & Williamson (1997). In the case of a tethered sphere undergoing VIV, besides Re, several other non-dimensional parameters are important such as (i) the reduced velocity, $U^* = U_\infty/(f_N D)$, where f_N denotes the tethered sphere's natural frequency; (ii) the mass ratio, $m^* \equiv m/m_f$, defined as the ratio between the structural mass, m, and the displaced fluid mass, m_f; (iii) the normalised tether length, $L^* \equiv L/D$, defined as the ratio between the tether length, L, and the sphere diameter; and (iv) the damping factor, ζ.

In this work, we are especially interested in the range of $U^*(2 < U^* < 7)$ around which the onset of VIV of a tethered sphere occurs ($U^* \approx 4$). As the sphere starts to

oscillate, different oscillation modes have been identified with increasing reduced velocity. Of particular interest to this research are the periodic modes I and II at relatively low U^* that are both associated with classic 'lock-in' of the sphere vortex shedding frequency with f_N (Jauvtis, Govardhan & Williamson 2001). Note that the transition between modes I and II is associated with a changing vortex phase, ϕ_v, defined as the phase difference between the vortex force and the transverse sphere displacement, and a jump in the total phase, ϕ_t, defined as the phase difference between the total transverse force and the transverse sphere displacement (Govardhan & Williamson 2005). These phase changes point at the close coupling between sphere displacement and vortex shedding. The highest transverse oscillation amplitudes (of the order of D) are obtained in mode II.

Planar particle image velocimetry (PIV) measurements by Govardhan & Williamson (2005) showed that, in the 'lock-in' region (modes I and II), transverse fluid forcing on the sphere was the result of a train of alternately shed hairpin vortices exhibiting a symmetry plane perpendicular to gravity. These hairpin vortices expelled fluid in alternating transverse directions and in accordance with Newton's third law, the fluid applied a reaction force (so-called vortex force) of equal but opposite sign on the sphere, much like wing tip vortices behind airplanes (Govardhan & Williamson 2005). More recent studies, using (high-speed) planar PIV and tomographic PIV (tomo-PIV) have further confirmed this mechanism (van Hout, Krakovich & Gottlieb 2010; Eshbal, Krakovich & van Hout 2012; van Hout, Katz & Greenblatt 2013*b*; Krakovich, Eshbal & van Hout 2013; Sareen *et al.* 2018; Eshbal *et al.* 2019*a*). Depending on the system properties, such as f_N, D and U_∞, Re can be relatively small and lie in the range $200 < Re < 800$. Therefore, prior to the onset of VIV ($U^* < 4$), the tethered sphere's wake is expected to be characterised by periodically shed hairpins having the same orientation and a single plane of symmetry as in the case of a stationary sphere (Johnson & Patel 1999; Eshbal *et al.* 2019*b*). Since no net forces perpendicular to the plane of symmetry are exerted on the sphere, it remains stationary, and the onset of VIV (at $U^* \approx 4$) must be the result of symmetry breaking. Recently, there has been interest in symmetry breaking of wakes behind bluff bodies. Chrust, Goujon-Durand & Wesfreid (2013) found that, for a fixed sphere, the critical Re above which the flow loses planar symmetry was approximately $Re \approx 375$, in good agreement with numerical results by Mittal (1999). The loss of planar symmetry at these low Re is accompanied by small-scale variations in the azimuthal angle of vortex formation. Szaltys *et al.* (2011) experimentally studied the nonlinear evolution of instabilities behind fixed spheres and disks through a modal decomposition of the streamwise vorticity for Re up to 450 (sphere) and 500 (for the disk). They showed that, for the sphere, axisymmetry was lost at $Re = 212$, and the onset of time dependence occurred at $Re = 268$, i.e. close to the well-accepted value of $Re \approx 270$. Grandemange, Cadot & Gohlke (2012) reported on reflectional symmetry breaking of a laminar 3-D wake which persisted even at large Re and led to a bistable turbulent wake. In a subsequent study, Grandemange, Gohlke & Cadot (2014) showed that, even when the instantaneous velocity deficit centroid of the turbulent sphere wake tended to be off the symmetry axis, in the absence of azimuthal disturbances, statistically all possible azimuths were equally explored. Upon introducing azimuthal disturbances, the wake 'selected' one or several preferred orientations. In the case of a tethered sphere, symmetry breaking is expected to lead to small fluctuating forces acting on the sphere that through mutual reinforcement between sphere displacement and vortex shedding will lead to VIV.

Relatively few numerical simulations have been performed on VIV of spheres having multiple degrees of freedom. Unlike experiments, an advantage of numerical simulations is that Re and U^* can be independently fixed. Numerical simulations at different, fixed Re

were performed by Rajamuni, Thompson & Hourigan (2018, 2020). Increasing Re widened the synchronisation (lock-in) region and increased the transverse response amplitude (up to $Re = 2000$). However, the topology of the wake structure remained the same as that measured at much higher Reynolds numbers (Govardhan & Williamson 2005). Behara, Borazjani & Sotiropoulos (2011) and Behara & Sotiropoulos (2016) solved the unsteady, incompressible Navier–Stokes equations for the flow coupled with the Lagrangian sphere motion equations using an immersed boundary approach for an elastically mounted sphere having three linear degrees of freedom (no rotation). Note that this allowed full 3-D movement, unlike a tethered sphere whose motion is restricted to a 2-D spherical surface. Behara *et al.* (2011) kept $Re(= 300)$ fixed and showed that, for a heavy sphere ($m^* = 2$), two distinct transverse response modes, a hairpin and a spiral mode, were observed in the range $4 < U^* < 9$. In the hairpin mode, the sphere moved along a linear transverse path while in the spiral mode, it moved along a circular path. 'Lock-in' regimes extended to larger U^* ranges in the spiral mode (Behara & Sotiropoulos 2016). Wake modes and associated sphere trajectories strongly depended on Re with spiral vortices being shed up to $Re \approx 500$ transitioning to hairpin vortex shedding in the range $500 < Re < 600$. For $Re > 600$, sphere oscillation became non-stationary.

Lee, Hourigan & Thompson (2013) and Rajamuni *et al.* (2020) performed numerical simulations of VIV of a neutrally buoyant ($m^* = 1$), and a light ($m^* = 0.8$) tethered sphere, respectively. Lee *et al.* (2013) covered a Re range of $50 \leq Re \leq 800$, corresponding to a narrow range of reduced velocities, $34 \leq U^* \leq 44$, while Rajamuni *et al.* (2020) fixed $Re(= 500$, 1200 and 2000) while changing the reduced velocity ($3 \leq U^* \leq 32$). Results of Lee *et al.* (2013) indicated that axisymmetry of the sphere wake was lost at $Re \approx 210$ and a two-threaded steady wake was observed in agreement with results for a stationary sphere (Johnson & Patel 1999). They further showed that the sphere started to vibrate at $Re \approx 270$, i.e. at the same critical Re as for a stationary sphere, indicating that the ability of the sphere to move did not affect the onset of unsteadiness. At $Re \approx 280$, planar symmetry was broken and vibration shifted to the azimuthal direction. In total, they defined seven different regimes spanning a wide Re range, $50 \leq Re \leq 12\,000$, where the high Re regimes were based on experimental sphere tracking experiments. Rajamuni *et al.* (2020) found that increasing Re increased the transverse amplitude response, especially for mode II.

All of the above discussed studies have been performed under steady upstream flow conditions, and an important question that has not been answered is 'what is the chain of events leading to VIV of a tethered sphere?' In addition, except for the tomo-PIV measurements by Eshbal *et al.* (2019*a*), no experimental information is available on the instantaneous, 3-D flow field in the wake of a tethered sphere. The goal of the present study is to simultaneously track the motion of a heavy, tethered sphere as well as the sphere wake's dynamic flow topology (i) before and after the onset of VIV under steady upstream flow conditions, and (ii) under transient upstream flow conditions while crossing the onset of VIV. These measurements provide much needed insight into the changes that the wake undergoes as VIV are initiated as well as on the associated transverse forcing on the sphere.

The transient flow conditions were imposed by stepwise changing U^* from 2.2 to 4.5, i.e. crossing the Hopf bifurcation. This allowed us to continuously follow any changes in the wake flow as the sphere crossed the onset of VIV. This research is part of an ongoing effort of our group to elucidate the 3-D vortex shedding in the wake of stationary spheres as well as in the wakes of tethered spheres undergoing VIV. The experimental set-up and data processing is succinctly described in § 2, results in § 3 and a summary and discussion is presented in § 4.

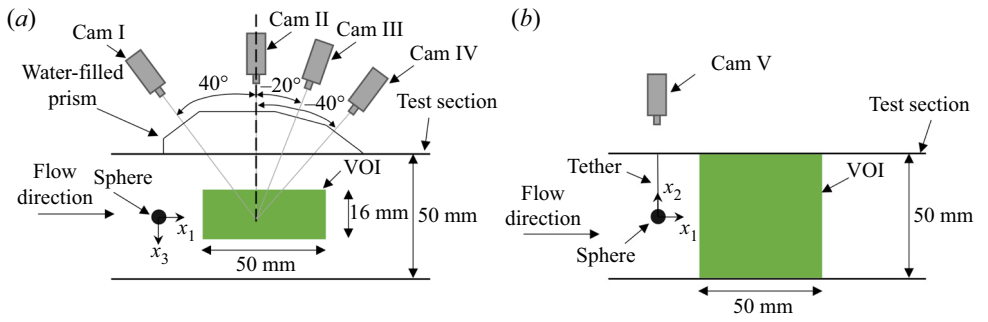

Figure 1. Schematic layout of set-up (not to scale). (*a*) Tomo-PIV (top view), (*b*) sphere tracking (side view). Employed coordinate system and VOI are also indicated.

2. Experimental system and data processing

The present experiments were performed in a closed-loop water tunnel (cross-section 50 × 50 mm^2), described in detail by Eshbal *et al.* (2019*a*). A stainless steel sphere ($D = 5.97 \pm 0.05$ mm, $m^* = 7.77 \pm 0.05$) was tethered to the top of the test section using a nylon monofilament (diameter $d = 70$ μm, tether length $L = 16.8 \pm 0.1$ mm, i.e. $L^* = L/D = 3.3 \pm 0.1$). The natural frequency of the tethered sphere including added mass (Govardhan & Williamson 2005) was $f_N = (1/2\pi)\sqrt{(g/L)((m^* - 1)/(m^* + C_A))} = 3.21 \pm 0.02$ Hz, where g is the gravitational acceleration, and $C_A = 0.5$ is the added mass coefficient for a sphere. The damping factor equalled $\zeta = 0.025 \pm 0.003$, based on free decay measurements. Note that the present measurements were performed using a similar sphere (material and size) as that used by van Hout *et al.* (2010) and Eshbal *et al.* (2019*a*). However, in the present case, attachment of the tether to the upper tunnel wall was different and, together with small changes in the sphere's mass and tether length, resulted in a slightly different f_N and damping factor. In the experiments by van Hout *et al.* (2010) and Eshbal *et al.* (2019*a*), the tether was attached to the upper part of the acrylic lid by passing it through a hole and keeping it in place by a piece of adhesive tape. Furthermore, van Hout *et al.* (2010) used a human hair as tether ($d = 58$ μm) while Eshbal *et al.* (2019*a*) used a nylon filament ($d = 70$ μm). In the current study, the tether was tied to the eye of a sewing needle that was tightly fit in the acrylic lid's hole such that the tether's attachment point was flush with the bottom of the lid. The tether was attached to the sphere by drilling a small hole into it, filling the hole with glue, and inserting the tether after which the glue was made to harden. In this way, kinks in the tether near the attachment point as well as glue protrusions from the sphere's surface were avoided. In addition, the tomo-PIV measurements reported by Eshbal *et al.* (2019*a*) focused on the 'far wake' of the sphere and were acquired within a volume located 4D downstream of the sphere while in the current measurements the start of the volume of interest (VOI) was located 0.8D downstream of the sphere centroid (when at rest). A right-handed Cartesian coordinate system with its origin at the sphere centre (when at rest) was adopted as shown in figure 1, where $x_i (i = 1, 2, 3)$ denote the streamwise and both transverse directions, respectively; U_i denote the corresponding instantaneous flow velocities. Vectors and tensors are printed in bold typeface, and a prime, '..′', denotes the root mean square (r.m.s.) value.

The flow field downstream of the tethered sphere was measured using a tomo-PIV system (LaVision GmbH) consisting of four CCD cameras (Imager SX 4M, 2360 × 1776 pixels, an Nd:YAG laser (Quantel 532 nm, max. 120 mJ at 15 Hz), laser volume optics and a water prism to reduce image distortion due to refraction (see figure 1*a*).

The illuminated VOI was $50 \times 50 \times 16\ \text{mm}^3$ (length $\times$ height $\times$ width), positioned $0.8D$ downstream of the sphere's centroid position when at rest. The cameras were arranged in a 'line set-up' (Adrian & Westerweel 2011) placed at angles of 40°, 0°, -20° and -40° (figure 1) relative to a line perpendicular to the flow direction. Cameras were equipped with Scheimpflug adapters to ensure good focus across the field of view and lenses having a focal length of 105 mm (Nikon, MicroNikkor). An f-number (defined as the ratio between the focal length of the lens and the diameter of its clear aperture) of 22 was used to ensure focus across the depth of the VOI.

Prior to the start of the measurements, calibration was performed across the whole depth of the VOI in 9 planes spaced 2 mm apart, using a dual-plane calibration plate (LaVision, Type 22). The sphere's translational motion was tracked using a 5th CCD camera (Imager Pro 4M, 2048×2048 pixels) that captured the sphere's centre position from the top (figure 1*b*), while ensuring synchronisation between sphere tracking and flow field measurements.

In the current research, several sets of tomo-PIV measurements were performed for steady upstream flow conditions at $U^* = 1.9$, 3.2, 4.5 and 7.2 (± 0.1 in all cases) corresponding to $Re = 230, 383, 532$ and 850 ($\pm 2.5\%$ in all cases), respectively. In addition to steady upstream flow conditions, data were also acquired for transient upstream flow conditions by stepwise changing U^* from 2.2 to 4.5 corresponding to $263 < Re < 532$. In total, five data sets were acquired at 15 Hz (four at steady and one at transient upstream flow conditions). Note that, in experiments, unlike numerical studies (Behara *et al.* 2011), Re and U^* are coupled for a given fluid–tether–sphere combination. The present range of Re was chosen to ensure that the vortex shedding in the wake of the sphere was characterised by large-scale vortices without the break-up and fragmentation observed at higher Re as a result of instabilities (Sakamoto & Haniu 1990). This enables the accurate measurement (given the limited spatial and temporal measurement resolution) of the 3-D vortex shedding topology. Since increasing Re does not strongly affect the large-scale vortex shedding topology in the synchronisation regime (Rajamuni *et al.* 2018, 2020) and the present tethered sphere's amplitude response is similar as that obtained at higher Re (e.g. Govardhan & Williamson 2005), we are confident that our results will also be relevant at a higher Reynolds number range. For the transient case, measurements were initiated at $U^* = 2.2$ and every 3.3 s (50 frames), U^* was stepwise increased by $\Delta U^* = 0.15$ until $U^* = 4.5$ was reached at $t^* = tU_\infty/D = 718$, after which data acquisition continued until $t^* = 1442$. Note that we investigated the effect of changing the time duration between steps (within a limited range) on the sphere's amplitude response and did not detect great sensitivity to it (not shown here). In all cases, the onset of VIV occurred after reaching the final value of $U^* = 4.5$. Small differences in the rate of increase of the sphere's amplitude response were attributed to random variability between experiments. Therefore, the chosen time duration between steps was a trade-off between the observed insensitivity of the response of the sphere to this, and the amount of data that could be processed.

Data processing of the sphere tracking results (Camera V) and the tomo-PIV images (Cameras I to IV) was different. Images containing the sphere were processed by multi-step, iterative image processing similar as by van Hout *et al.* (2010) and described in the following. An example, cropped raw image containing the sphere is depicted in figure 2(*a*). The raw image was first converted to a binary image by thresholding (figure 2*b*). Next, small objects were filtered based on size (figure 2*c*) and the boundary of the sphere was detected as the first encountered 'white' pixel (encircled by a red circle in figure 2*d*) after which the remaining boundary pixels were detected (shown as the red curve in figure 2*d*). Based on the detected sphere boundary points, the sphere

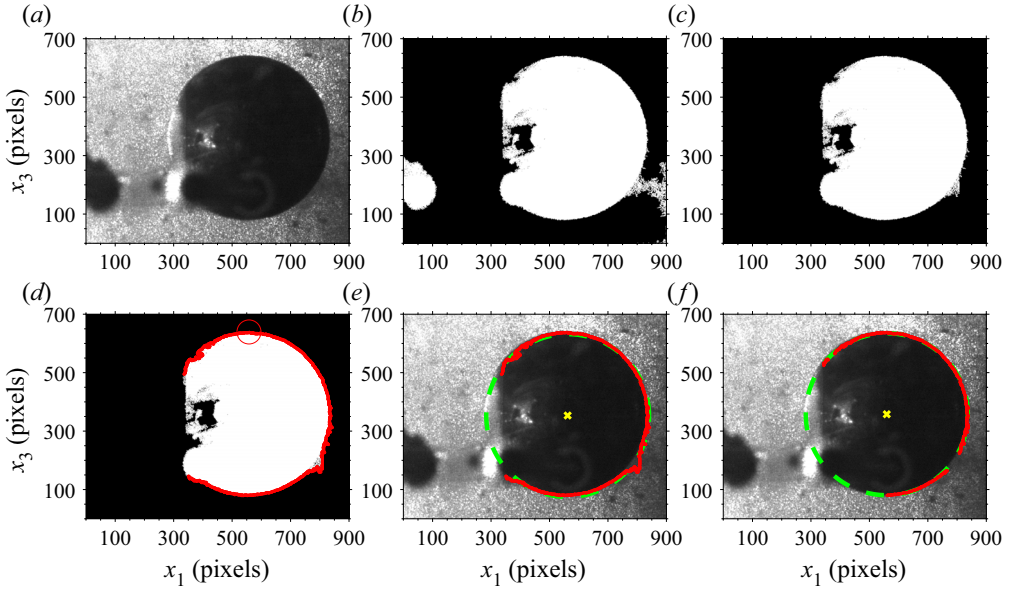

Figure 2. Overview of the different steps in the sphere centroid detection algorithm illustrated for an instantaneous cropped image containing the sphere; (*a*) raw data, (*b*) thresholded, (*c*) after small 'blob' removal, (*d*) detection of first point on the sphere boundary (indicated by red circle) and all points belonging to the sphere's edge (red curve), (*e*) first estimate of sphere centroid (perimeter indicated by green dash circle), (*f*) final result of the iterative least-squares fit procedure. The yellow × symbol in (*e*) and (*f*) denotes the determined sphere centroid based on the estimated sphere radius.

radius as well as the sphere centroid position was estimated by a least-squares fitted circle (sphere perimeter denoted by a green dash circle and its centroid by a yellow × symbol in figure 2*e*). This procedure was iteratively repeated while discarding detected sphere boundary points that exceed one standard deviation of the radius estimated in the previous iteration (figure 2*f*). The algorithm was repeated until the coordinates of the sphere's centroid position converged to within 0.01 pixel. By applying this method, sub-pixel accuracy (±0.6 pixels) was achieved. Note that the accuracy of the applied procedure was verified by applying the algorithm to an exact circle as well as several circles with artificially added noise. Given the present imaging resolution of 94.1 pixels mm^{-1}, the measurement uncertainty was $\pm 0.001D$. This data processing procedure resulted in time series of the sphere centroid position, $x_{i,c}(t^*)$, where the subscript 'c' denotes 'centroid'. In order to characterise the tethered sphere's streamwise and transverse amplitude response, normalised r.m.s. amplitudes based on the sphere centroid positions were determined by: $A_i^* = \sqrt{2}x'_{i,c}/D$, for $i = 1, 3$.

Data processing of the tomo-PIV images was similar to that employed by Eshbal *et al.* (2019*b*). Three-dimensional vector maps were obtained by multi-pass, 3-D cross-correlation (DaVis 8.4, LaVision GmbH) with a final interrogation volume size of $56 \times 56 \times 56$ voxels with 75 % overlap, corresponding to a vector spacing of 0.22 mm ($0.037D$). Between passes, universal outlier detection based on a median filter was performed (Westerweel & Scarano 2005) while at the end of each pass, a $3 \times 3 \times 3$ Gaussian smoothing filter was applied. The resulting vector maps were further spatially smoothed using a quadratic regression over 15 points in each direction (Elsinga *et al.* 2010) corresponding to $0.5D$. This is not expected to remove any relevant large-scale flow structures in the sphere wake. Spatial velocity gradients were based on the locally fitted

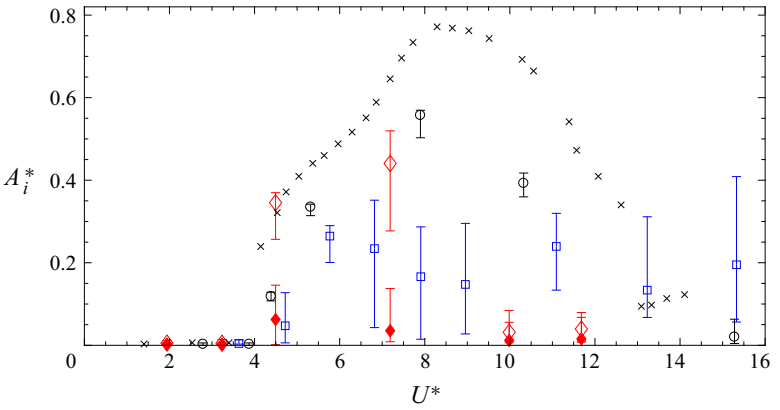

Figure 3. Normalised transverse amplitude as a function of the reduced velocity. Present data: $m^* = 7.77$, $(m^* + C_A)\zeta = 0.207$: $i = 3$ ($\diamond$ – red, and 1 ($\blacklozenge$ – red); Literature data ($i = 3$): $\square$ – blue (Eshbal *et al.* 2019*a*) $m^* = 7.77$, $(m^* + C_A)\zeta = 0.428$, $\circ$ (Krakovich *et al.* 2013) $m^* = 7.87$, $(m^* + C_A)\zeta = 0.167$, $\times$ (Govardhan & Williamson 2005) $m^* = 2.8$, $(m^* + C_A)\zeta = 0.029$. Vertical bars denote extreme values.

quadratic regression (Elsinga *et al.* 2010), and the data quality was assessed by evaluating the residual of the continuity equation for an incompressible fluid, $\partial U_i/\partial x_i = 0$ (R^2 values exceeded 0.87, see also van Hout *et al.* 2018).

In the following, instantaneous vortices are visualised as iso-surfaces of the Q-criterion (Hunt, Wray & Moin 1988) that defines vortices as regions where the magnitude of the rate-of-rotation exceeds that of the rate-of-strain, $Q = \frac{1}{2}(\|\boldsymbol{\Omega}\|^2 - \|\boldsymbol{S}\|^2) > 0$. Here, $S_{ij} = \frac{1}{2}(\partial U_i/\partial x_j + \partial U_j/\partial x_i)$ defines the rate-of-strain tensor, and $\Omega_{ij} = \frac{1}{2}(\partial U_i/\partial x_j - \partial U_j/\partial x_i)$ defines the rate-of-rotation tensor; $\|..\|$ denotes the norm of a tensor, e.g. $\|\boldsymbol{\Omega}\| = [tr(\boldsymbol{\Omega}\boldsymbol{\Omega}^T)]^{1/2}$, where tr denotes the trace of the tensor. The iso-surfaces are overlaid by the components of the normalised vorticity, $\omega_i^* = \omega_i D/U_\infty$, where $\omega_i = \partial U_k/\partial x_j - \partial U_j/\partial x_k$ (i, j, k are dummy indices).

3. Sphere and wake dynamics: steady conditions

The normalised streamwise and transverse r.m.s. amplitudes, $A_i^*(i = 1, 3)$, of the tethered sphere under steady upstream flow conditions are plotted in figure 3 in the range $0 < U^* < 16$, together with relevant literature data for heavy tethered spheres. Note that differences in the transverse amplitude response reported in prior work of our group (van Hout *et al.* 2010; Krakovich *et al.* 2013; Eshbal *et al.* 2019*a*) for a stainless steel sphere with similar m^* and L^* are mainly due to different values of ζ that changed as a result of the way the tether was attached to the upper channel wall (see § 2). As discussed by Govardhan & Williamson (2005), increasing the mass-damping parameter, $(m^* + C_A)\zeta$, beyond 0.02 narrows the width of the lock-in region (modes I and II) and reduces the peak response value of A_3^* below its saturation value of 0.9. For example, when $(m^* + C_A)\zeta = 0.428$ (Eshbal *et al.* 2019*a*) the normalised transverse r.m.s. amplitude did not exceed $A_3^* = 0.35$ (at $U^* = 5.5$), while for $(m^* + C_A)\zeta = 0.167$ (Krakovich *et al.* 2013), A_3^* reached 0.55 at $U^* \approx 8$ (mode II). In the present measurements, ζ was slightly larger than in Krakovich *et al.* (2013), which narrowed the synchronisation region (see figure 3). Note that the peak amplitude response corresponds well to those in the Griffin plot (A_3^* vs $(m^* + C_A)\zeta$) reported by Govardhan & Williamson (2005).

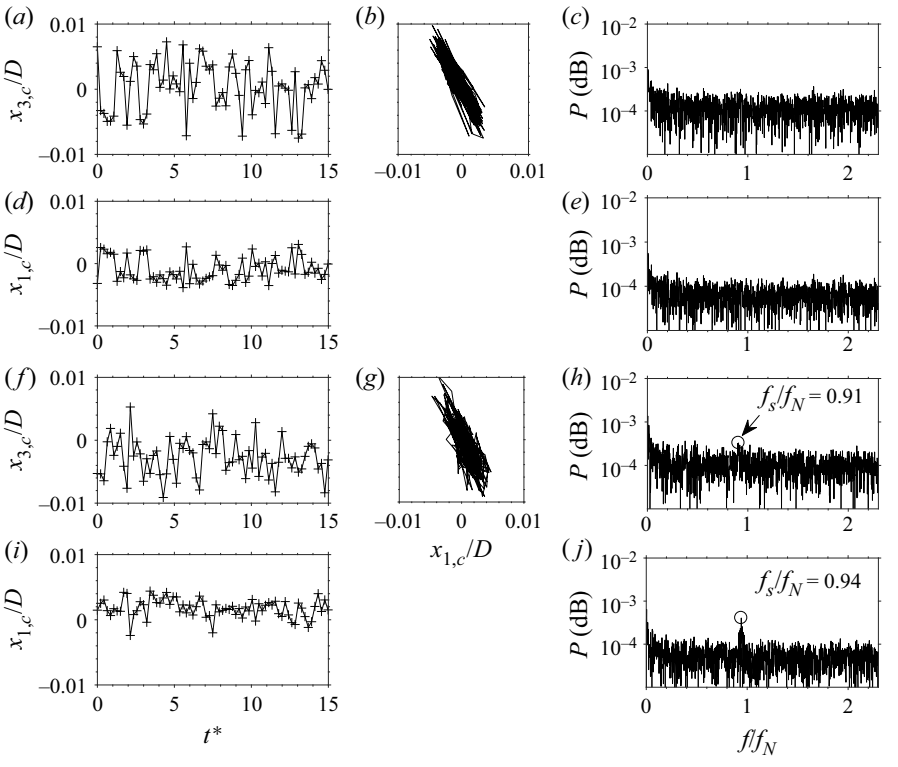

Figure 4. VIV response of the tethered sphere under steady upstream flow conditions at $U^* = 1.9$ (*a–e*) and $U^* = 3.2$ (*f–j*). (*a*,*d*,*f*,*i*) Examples of normalised sphere centroid positions for $0 < t^* < 15$: (*a*,*f*) $x_{3,c}/D$ and (*d*,*i*) $x_{1,c}/D$; (*c*,*e*,*h*,*j*) associated power spectra; (*b*,*g*) phase diagrams of sphere centroids in the x_1–x_3 plane for $U^* =$ (*b*) 1.9 and (*g*) 3.2.

In addition to A_3^*, the normalised streamwise r.m.s. amplitude, A_1^*, is also plotted in figure 3 for the present measurements. As expected for a heavy tethered sphere, values of A_1^* remain low and do not exceed $A_1^* = 0.06$ (at $U^* = 4.5$). Here, we are interested in the changing vortex shedding as the sphere crosses the onset of VIV, and we will focus on $U^* = 1.9$, 3.2, 4.5 and 7.2 in §§ 3.1 and 3.2.

3.1. *Prior to the onset of VIV: $U^* = 1.9$ and 3.2*

The tracked streamwise and transverse sphere centroid positions, associated power spectra and phase diagrams depicting the sphere centroid positions in the x_1–x_3 plane, are shown in figure 4. It is interesting to see that, in both cases ($U^* = 1.9$ and 3.2), the sphere is not completely stationary (figure 4*a*,*d*,*f*,*i*), and, although displacements are small (up to $|0.01D|$), for $U^* = 3.2$ (figure 4*f–j*) the power spectrum based on the time series of $x_{1,c}$ (figure 4*j*) displays a small but distinct peak at $f_s/f_N = 0.94$, where f_s denotes the sphere oscillation frequency. This indicates that, at $U^* = 3.2(Re = 383)$, sphere oscillations in the streamwise direction 'lock-in' to the natural frequency. Note that in the transverse direction, the power spectrum (figure 4*h*) shows only a very small peak (pointed at by the arrow in figure 4*h*) almost indistinct from the noise level. For $U^* = 1.9$, the power spectra (figure 4*c*,*e*) do not indicate any peaks that rise above the noise level.

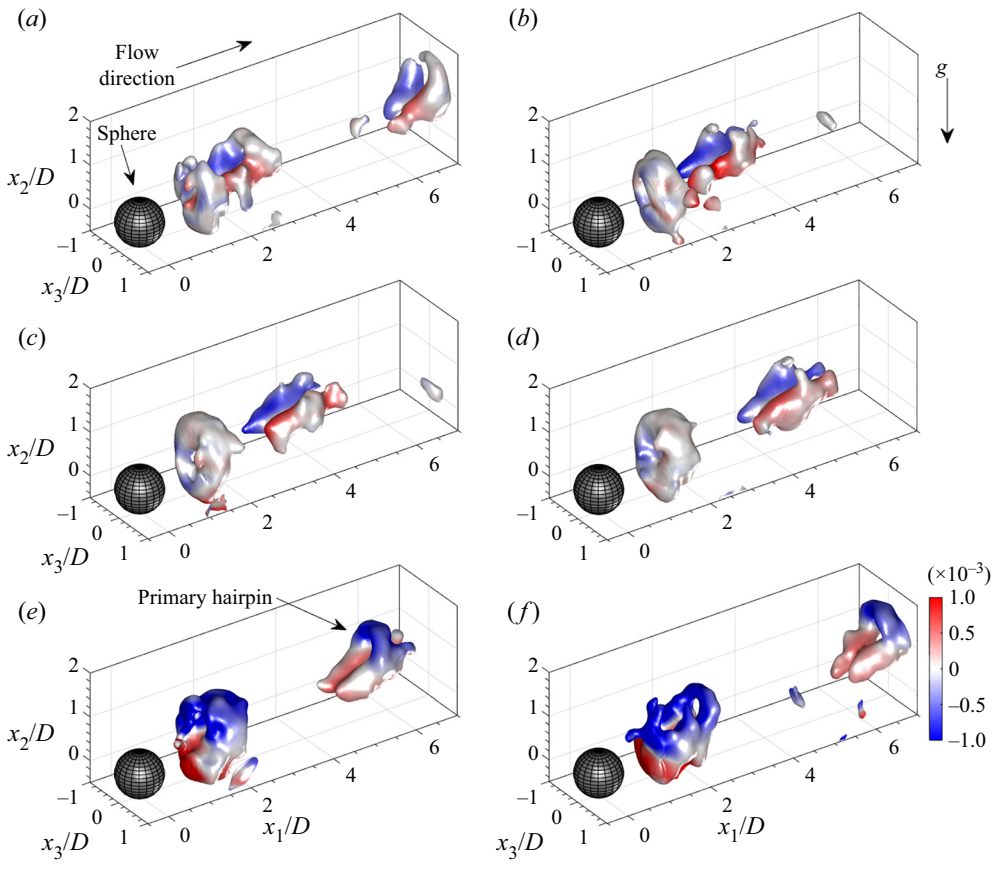

Figure 5. Sequence of snapshots (at one third of the actual temporal resolution, $\Delta t^* = 1.24$) of the instantaneous vortex structure visualised by iso-surfaces of the Q-criterion overlaid by ω_1^* (*a–d*) and ω_3^* (*e*,*f*). Here, $U^* = 1.9$, $Re = 230$. Link to supplementary movie 'Fig 5.mp4' is available at https://doi.org/10.1017/jfm.2022.428. Arrow next to g denotes direction of gravity.

In order to investigate the generated vortices in the wake of the tethered sphere prior to the onset of VIV, the 3-D vortex shedding measured at $U^* = 1.9(Re = 230)$ and $3.2(Re = 383)$ under steady upstream flow conditions is presented in figures 5 and 6 (see also associated supplementary movies 'Fig 5.mp4' and 'Fig 6.mp4'). These figures depict sequences of snapshots of the vortices in the wake of the tethered sphere as visualised by iso-surfaces of the Q-criterion overlaid by the normalised streamwise and transverse vorticity components. Focusing first on the vortices in the wake of the sphere at $U^* = 1.9(Re = 230$, figure 5), unsteady vortex shedding is observed. This was unexpected at such a low Re and differs from that reported for a fixed sphere immersed in a steady uniform flow (Johnson & Patel 1999; Szaltys *et al.* 2011) as well as for a neutrally buoyant tethered sphere (DNS, Lee *et al.* 2013). For a fixed sphere, it has been reported that wake axisymmetry is lost at $Re \approx 210$ and a 'double-threaded' steady wake (Magarvey & MacLatchy 1965; Johnson & Patel 1999; Ormières & Provansal 1999; Tomboulides & Orszag 2000; Szaltys *et al.* 2011) appears up to $Re \approx 270$, beyond which unsteady vortex shedding in the form of hairpins occurs. We surmise that, for the present case, the observed unsteadiness is due to the use of a tether that allows constraint sphere movement. Even small disturbances in the upstream flow induce small sphere movements (see

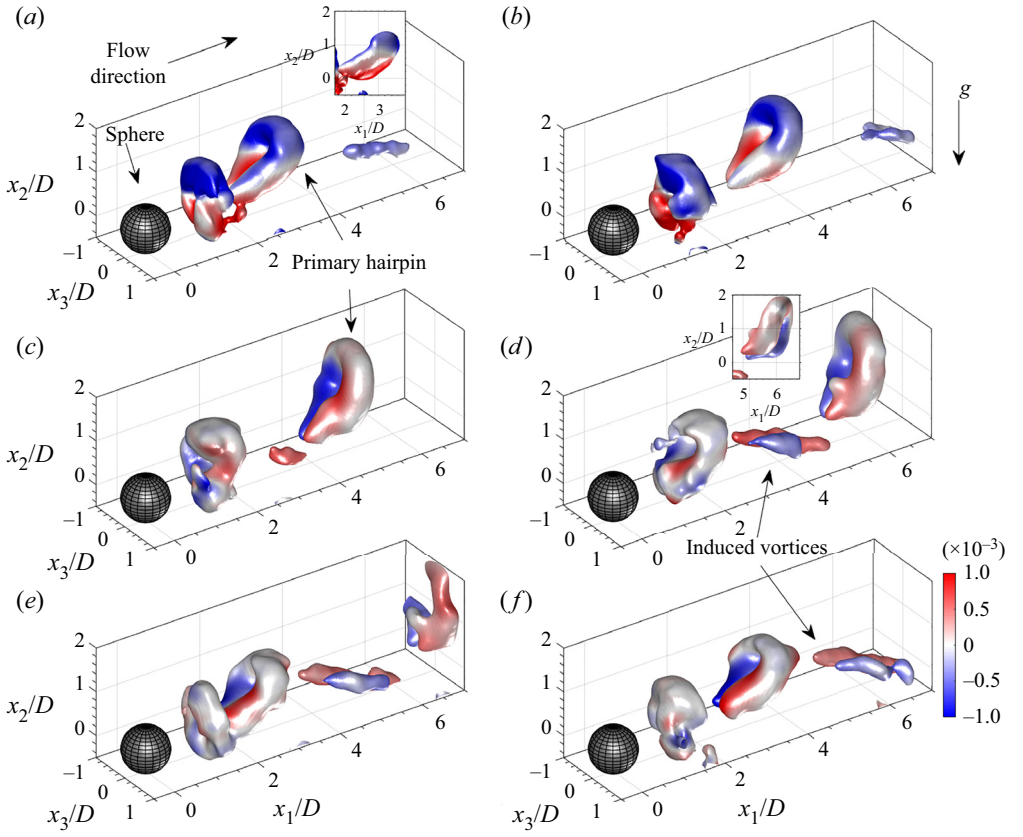

Figure 6. Sequence of snapshots (at half the actual temporal resolution, $\Delta t^* = 1.38$) of the instantaneous vortex structure visualised by iso-surfaces of the Q-criterion overlaid by ω_3^* (*a*,*b*) and ω_1^* (*c*–*f*). Here, $U^* = 3.2$, $Re = 383$. Link to supplementary movie 'Fig 6.mp4' available at https://doi.org/10.1017/jfm.2022.428. Insets in (*a*) and (*d*) depict side views of the primary hairpins. Arrow next to g denotes direction of gravity.

figure 4*a*,*d*,*f*,*i*) that introduce azimuthal disturbances close to the point where the tether is attached to the sphere and the boundary layer separates. As a result, we surmise that the double-threaded wake becomes unstable and develops into unsteady vortex shedding at a lower Re than for a fixed sphere. This mechanism also ensures that the generated primary hairpin vortices are shed with their 'heads' pointing upwards in the direction of the tether (see figure 5*e*). Note that time-resolved, planar PIV measurements performed by David *et al.* (2020) on a fixed smooth sphere at $Re = 226$ in the same facility did not exhibit unsteady vortex shedding, strengthening our point that the tethered sphere's ability to move is crucial. In the present measurements at $U^* = 1.9$, the ratio between the vortex shedding frequency, f_v (determined directly from the sequence of snapshots), and f_N equalled $f_v/f_N = 0.29$. This value is far from lock-in, which explains the lack of a distinct peak in the power spectra based on $x_{i,c}$ (figure 4*c*,*e*).

For both reduced velocities ($U^* = 1.9$ and 3.2 in figures 5 and 6, respectively), 'primary' hairpin vortices are shed with their 'heads' rotating in the clockwise direction ($\omega_3^* < 0$, figures 5*e*,*f* and 6*a*,*b*). The induced flow field due to the rotation of the hairpin legs causes the hairpins to 'lift up'. This is especially clear at $U^* = 3.2$ (figure 6) where the primary hairpin inclination angles measured from the horizontal, increase with increasing x_1/D from approximately 40° to 73° (see insets in figure 6*a*,*d*). Further downstream the hairpins

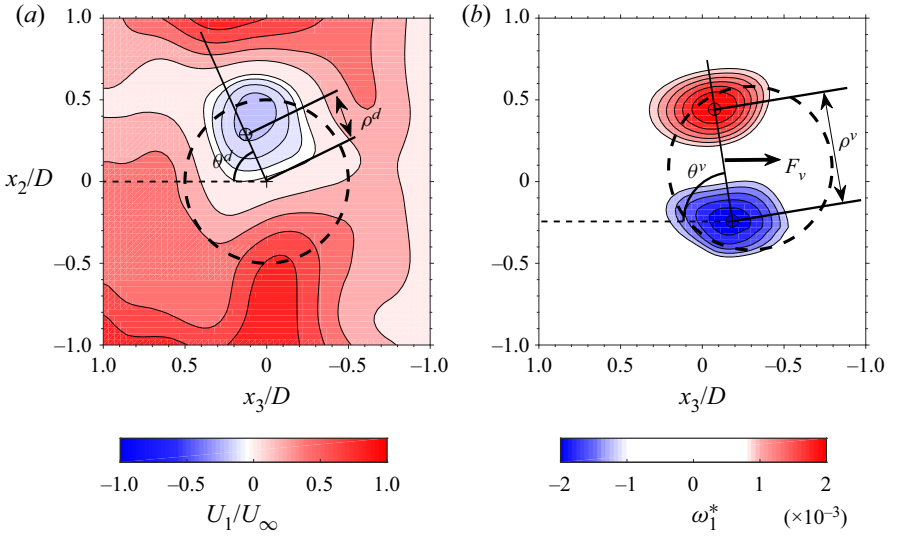

Figure 7. Definition of the angles and distances in a transverse plane at $x_1/D = 2$ associated with (*a*) the centroid position of the velocity deficit and (*b*) the orientation of the shed vortices. The dashed circle denotes the perimeter of the tethered sphere. The direction of the vector associated with F_v in (*b*) denotes the vortex force exerted on the fluid in the x_3-direction. Centroids are denoted by $\oplus$.

are expected to develop into vortex rings (Eshbal *et al.* 2019*a*). Note that, for $U^* = 1.9$ (figure 5), the arches spanning the transverse gap between the hairpin legs are weak and are not always observed in the Q-criterion iso-surfaces. However, contour plots of ω_3 in equatorial (x_1–x_2) planes (not shown) showed clear vorticity 'blobs' ($\omega_3^* < 0$) at the location of the presumed hairpin heads at all stages of vortex shedding.

For $U^* = 3.2$ ($Re = 383$, figure 6), 'primary' hairpin vortices were periodically shed at $f_v/f_N = 0.5$, i.e. closer to 'lock-in' (see power spectra in figure 4*h*,*j*). In contrast to $U^* = 1.9$, as the primary hairpins move downstream, the legs of secondary (or 'induced') vortices of opposite sign appear at $x_1/D \approx 3$ (see also Johnson & Patel 1999; Eshbal *et al.* 2019*b*). Note that, within the current extent of the VOI, they do not become fully developed hairpins. However, generation of the induced vortices doubles the vortex shedding frequency such that $f_v/f_N \approx 1$, in agreement with the frequency peak observed in the power spectrum associated with $x_{1,c}(t)$ (figure 4*j*). Furthermore, as the symmetry plane of the shed vortices is parallel to gravity, little forcing is expected to be imposed in the x_3-direction, explaining the lack of a distinct frequency peak in the power spectrum of $x_{3,c}(t)$ (figure 4*h*).

To obtain more insight into the vortex shedding dynamics, the instantaneous centroid position of the velocity deficit, $x_{i,c}^d (i = 2, 3)$, in a transverse plane downstream of the sphere (figure 7*a*) was determined by (Grandemange *et al.* 2014)

$$x_{i,c}^d/D = \frac{\displaystyle\iint_A \frac{x_i}{D}\left(1 - \frac{U_1}{U_\infty}\right) \mathrm{d}A}{\displaystyle\iint_A \left(1 - \frac{U_1}{U_\infty}\right) \mathrm{d}A}, \tag{3.1}$$

for $i = 2, 3$, where the superscript 'd' denotes 'associated with the velocity deficit'. Here, A is the integration domain (limited to $U_1/U_\infty < 0.5$) in the x_2–x_3 plane. The

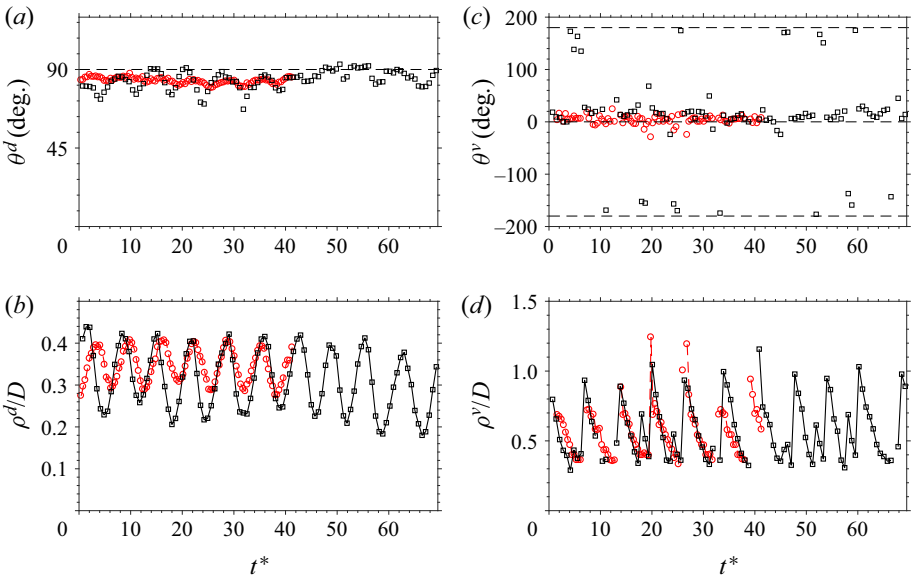

Figure 8. Instantaneous centroid positions of the velocity deficit (*a*,*b*) and the orientations and separation distances of the shed vortices (*c*,*d*) evaluated at a transverse plane located at $x_1/D = 2.0$ (see figure 7). (*a*) θ^d, (*b*) ρ^d/D, (*c*) θ^v, (*d*) ρ^v/D. Here, $U^* = 1.9$ (○ – red), 3.2 (□).

centroid positions of the velocity deficit relative to the (non-oscillating) sphere centre were characterised by their radial positions, ρ^d, and in-plane angles, θ^d (measured clockwise from the horizontal), as illustrated in figure 7(*a*).

In addition to $x^d_{i,c}/D$, changes in the orientation of the shed hairpins' symmetry plane are important to understand the onset of VIV (see also Chrust *et al.* 2013). This was studied here by determining the instantaneous relative position of the longitudinal, counter-rotating vortex 'legs' as they crossed the transverse plane at $x_1/D = 2$. An example contour plot showing two 'blobs' of opposite sign ω_1^* associated with the longitudinal vortices, is depicted in figure 7(*b*). Their relative position was defined by the angle, θ^v, and the distance between the centroids, ρ^v (see figure 7*b*), where the superscript 'v' denotes 'associated with the vortex legs'. The uncertainty of ρ^v was estimated as $\pm 0.04D$, i.e. twice the uncertainty associated with the 'blobs' centroid positions. Note that θ^v was measured from the negative vorticity blob to the positive one (figure 7*b*), and as a result, $\theta^v = 0^\circ$ corresponds to a symmetry plane parallel to gravity, whereas $\theta^v = \pm 90^\circ$ corresponds to one perpendicular to gravity.

Results for (θ^d, ρ^d/D) and (θ^v, ρ^v/D) are plotted in figure 8 for $U^* = 1.9$ and 3.2. For both U^*, θ^d (figure 8*a*) and ρ^d/D (figure 8*b*) oscillate at the primary vortex shedding frequency. Oscillation amplitudes increase with increasing U^*. The oscillations of θ^d indicate that the instantaneous wake (as characterised by the velocity deficit) exhibits small transverse deviations that increase with increasing U^* just prior to the onset of VIV.

The orientation of the symmetry plane of the vortices crossing the transverse plane is depicted in figure 8(*c*). For both U^*, θ^v mostly fluctuate around 0° since these represent the dominant primary hairpins crossing the transverse plane at $x_1/D = 2.0$. However, for $U^* = 3.2$, values of $\theta^v = \pm 180^\circ$ represent induced vortices whose rotation direction is flipped. Note that, although values of θ^v associated with $U^* = 3.2$ are more scattered around 0°, the shed vortices' symmetry planes are still predominantly in the direction

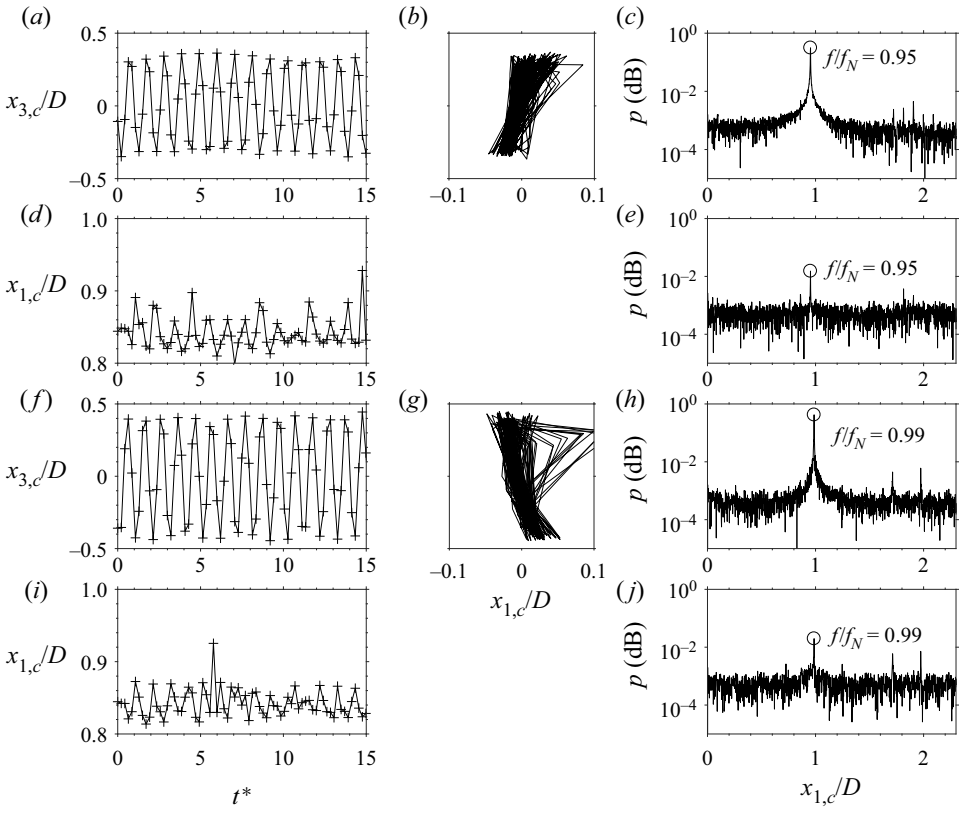

Figure 9. VIV response of the tethered sphere under steady upstream flow conditions at $U^* = 4.5$ (*a–e*) and $U^* = 7.2$ (*f–j*). (*a*,*d*,*f*,*i*) Examples of normalised sphere centroid positions for $0 < t^* < 15$: (*a*,*f*) $x_{3,c}/D$, and (*d*,*i*) $x_{1,c}/D$; (*c*,*e*,*h*,*j*) associated power spectra; (*b*,*g*) phase diagrams of sphere centroids in the x_1–x_3 plane for $U^* =$ (*b*) 4.5 and (*g*) 7.2.

of gravity. The distance between the legs of the shed vortices mostly fluctuates in the range $0.35 < \rho^v/D < 1.0$ (figure 8*d*). Maximum values of ρ^v/D obtained just after the hairpin head crosses the transverse plane, slightly precede those of ρ^d/D (figure 8*b*,*d*), more so for $U^* = 1.9$. As the hairpin vortex crosses the plane, ρ^v/D decreases (see for example figure 6*c*). Further downstream, the legs unite and a vortex ring is formed (figure 6*d*).

3.2. *Beyond the onset of VIV: $U^* = 4.5$ and 7.2*

Transverse and streamwise sphere centroid positions as a function of t^*, associated power spectra and phase diagrams are displayed in figure 9 for $U^* = 4.5$ (mode I) and 7.2 (mode II). Both fall within the synchronisation or 'lock-in' region (see figure 3) and $|x_{3,c}/D|$ reach approximately 0.3 and 0.4 for $U^* = 4.5$ and 7.2, respectively (figure 9*a*,*f*). Note that although the sampling frequency was sufficiently high to resolve periodicity (according to the Nyquist criterion), extreme values of $x_{3,c}/D$ are undersampled and fluctuate somewhat. Although streamwise oscillation amplitudes (figure 9*d*,*i*) have increased compared with those for $U^* = 1.9$ and 3.2 (figure 4*d*,*i*), they remain mostly below $0.04D$, i.e. an order of magnitude lower than in the transverse direction. Sphere trajectories in the x_1–x_3 plane depicted in figures 9(*b*) and 9(*g*), follow more or less linear paths at slightly changing orientation angles. For both U^*, the power spectra based on the time series of $x_{i,c}$ ($i = 1$,

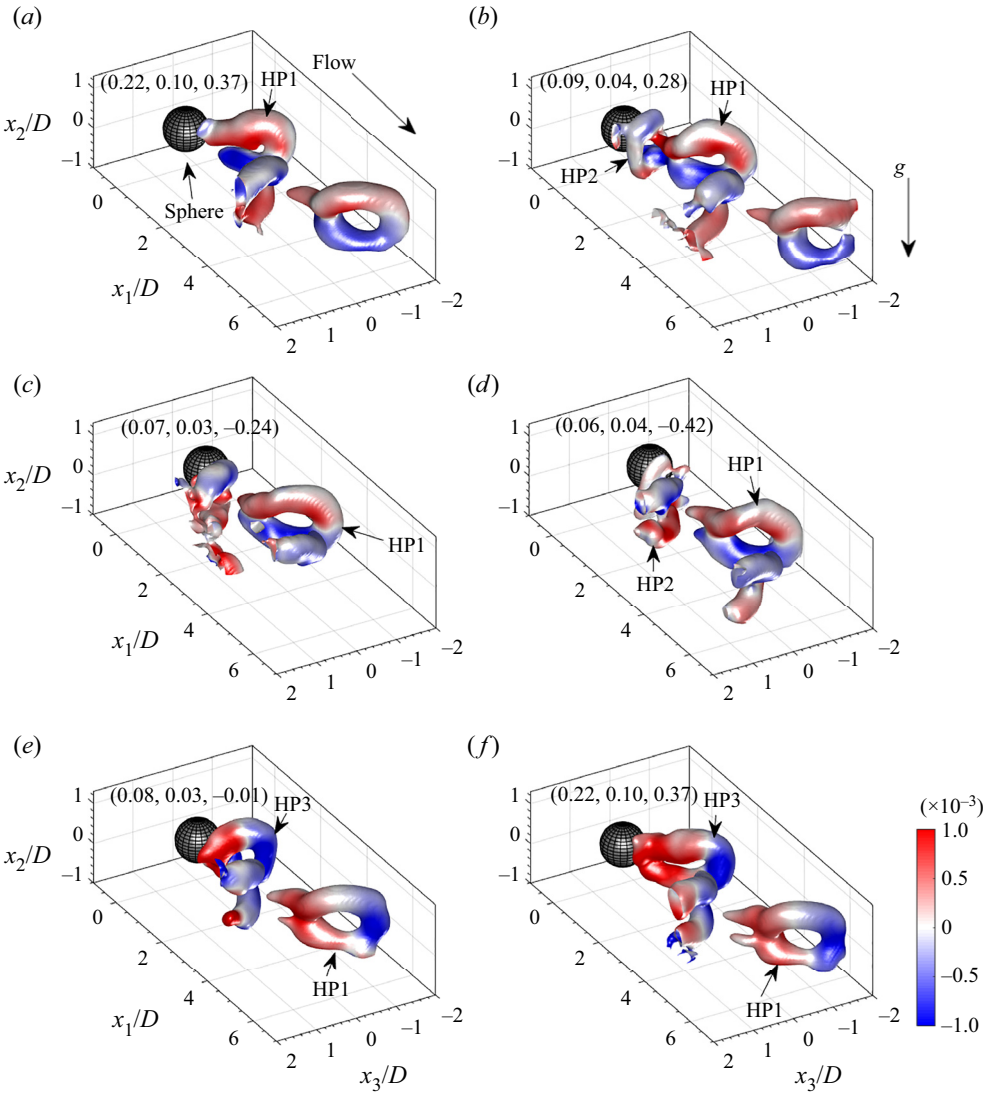

Figure 10. Sequence of snapshots (at actual temporal resolution, $\Delta t^* = 0.96$) of the instantaneous vortex structure in the wake of the tethered sphere undergoing VIV, $U^* = 4.5$, $Re = 532$. The structures are visualised by iso-surfaces of the Q-criterion and overlaid by ω_1^* (*a–d*) and ω_2^* (*e,f*). Link to supplementary movie 'Fig 10.mp4' available at https://doi.org/10.1017/jfm.2022.428. Values within parentheses denote the instantaneous sphere centroid positions, $(x_{1,c}/D, x_{2,c}/D, x_{3,c}/D)$. Arrow next to g denotes the direction of gravity.

3, figure 9*c,e,h,j*) indicate strong frequency peaks close to the natural frequency (a clear sign of 'lock-in') with $f_s/f_N = 0.95$ and 0.99 for $U^* = 4.5$ and 7.2, respectively.

Three-dimensional views of the vortex shedding sequence visualised by iso-surfaces of the Q-criterion and overlaid by ω_1^* and ω_2^* are depicted in figures 10 and 12 for $U^* = 4.5$ and 7.2, respectively. Associated top views are depicted in figures 11 and 13. Note that, due to the limited transverse extent of the VOI, the present measurements only fully capture one side of the vortex shedding sequence. However, since vortex shedding at $U^* = 4.5$ and 7.2 is symmetric about the x_1–x_2 plane ($x_3/D = 0$), the shedding sequence can be analysed using one side only. In contrast to $U^* = 1.9$ and 3.2 (figures 5 and 6), vortex shedding

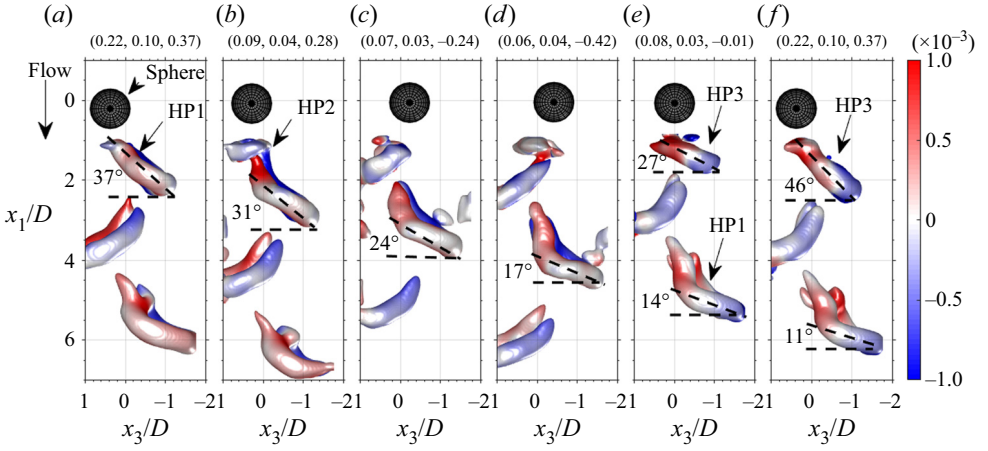

Figure 11. Top view of the same sequence of snapshots depicted in figure 10.

is now characterised by hairpin vortices exhibiting a symmetry plane perpendicular to gravity. The chain of events accompanying the change in the orientation of the symmetry plane as U^* is increased and VIV is initiated, is analysed and discussed in detail in § 4. The hairpin vortices provide the transverse forcing on the sphere in analogy with trailing wing tip vortices as discussed by Govardhan & Williamson (2005) and Eshbal *et al.* (2012) and further analysed in § 3.2.1.

We will first discuss the shedding and advection of the vortices in the wake of the tethered sphere for $U^* = 4.5$ (figures 10 and 11, see also the associated supplementary movie 'Fig 10.mp4'). Close to the sphere, a fully developed hairpin vortex (denoted by 'HP1' in figures 10 and 11) is observed as the sphere is close to its extreme transverse position ($x_{3,c}/D = 0.37$, figures 10*a* and 11*a*). In the next frame (figure 10*b*) as the sphere changes direction and moves towards the origin ($x_{3,c}/D = 0.28$ in figure 10*b*), the next hairpin vortex (denoted by 'HP2' in figures 10*b* and 11*b*) is generated. As HP1 is advected downstream and transitions into a vortex ring, the angle it makes with the transverse direction reduces from $37^\circ \pm 1^\circ$ to $11^\circ \pm 1^\circ$ as can be clearly observed in the top views depicted in figure 11. This changing orientation is the result of the unequal strength of the counter-rotating vortices comprising the vortex ring in the x_1–x_3 plane (at $x_2/D = 0$, not shown, see also Leweke, Le Dizes & Williamson 2016). In contrast, in the immediate proximity of the sphere, the orientation angle of HP3 increases upon shedding (figure 11*e*,*f*) as the head of HP3 is stretched due to its exposure to the fast moving incoming flow while its base is sheltered behind the sphere. The estimated advection velocity based on the tip positions of HP1 equalled $0.84U_\infty$ comparing well with the values reported by Krakovich *et al.* (2013).

As previously shown in the bifurcation diagram (figure 3), A_3^* was significantly higher for $U^* = 7.2$ than for $U^* = 4.5$. The sequence of 3-D plots of the instantaneous wake structure depicted in figures 12 and 13 shows how this is associated with a change in the vortex shedding pattern (see also associated supplementary movie 'Fig 12.mp4'). While for $U^* = 4.5$, two hairpin vortices were shed per oscillation cycle (figure 10), for $U^* = 7.2$ four were shed per cycle (figure 12). The shedding sequence for $U^* = 7.2$ is started as a hairpin vortex (denoted by 'HP4' in figures 12*a* and 13*a*) is generated when the sphere is moving in the negative x_3-direction. As the sphere is close to its extreme position ($x_{3,c}/D = -0.45$ in figures 12*b* and 13*b*) and HP4 detaches from it, a small hairpin head

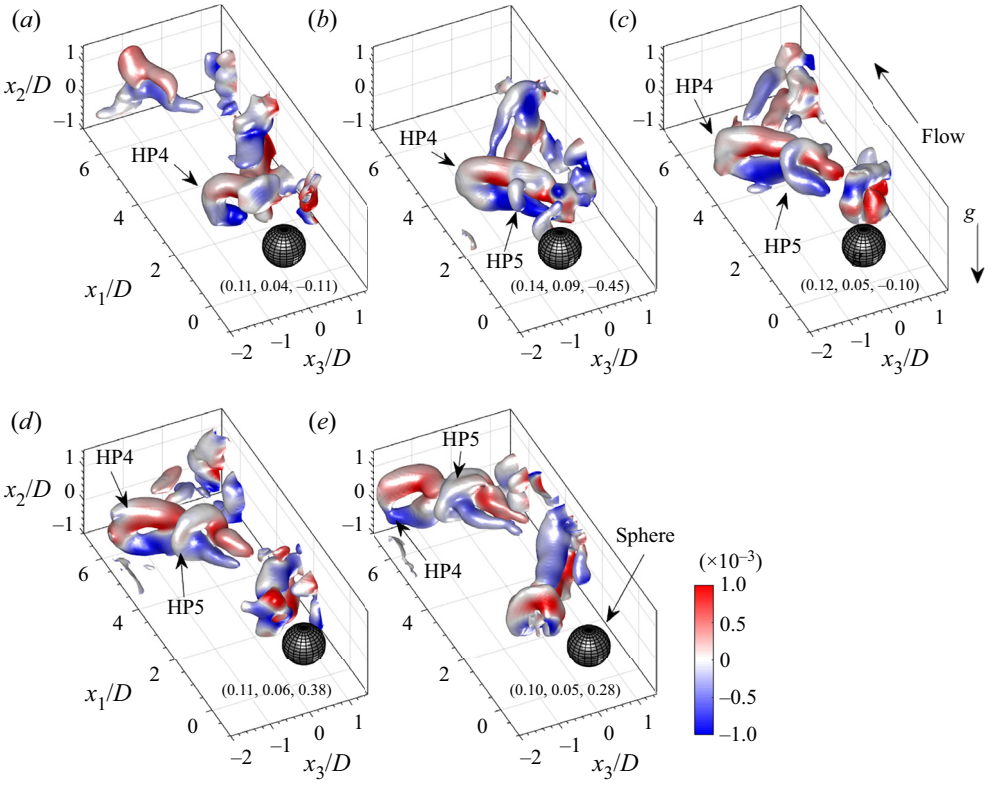

Figure 12. Sequence of snapshots (at actual temporal resolution, $\Delta t^* = 1.54$) of the instantaneous vortex structure in the wake of the tethered sphere undergoing VIV, $U^* = 7.2$, $Re = 850$. The structures are visualised by iso-surfaces of the Q-criterion overlaid by ω_1^*. Link to supplementary movie 'Fig 12.mp4' available at https://doi.org/10.1017/jfm.2022.428. Values within parentheses denote the instantaneous sphere position, $(x_{1,c}/D, x_{2,c}/D, x_{3,c}/D)$. Arrow next to g denotes the direction of gravity.

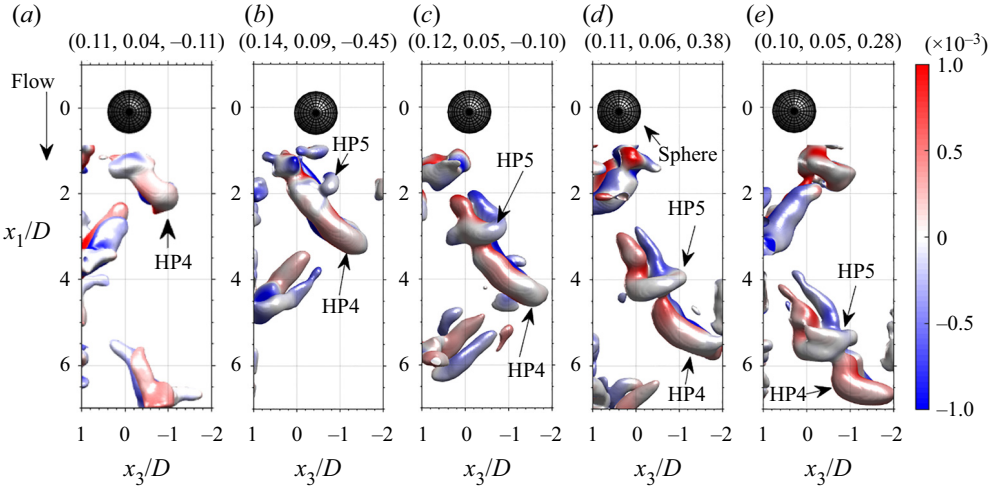

Figure 13. Top view of the same sequence of snapshots depicted in figure 12.

(denoted by 'HP5' in figures 12*b* and 13*b*) appears and bridges between the 'legs' of HP4. In subsequent snapshots (figures 12*c–e* and 13*c–e*), HP5 develops into a hairpin vortex while HP4 starts to resemble a vortex ring. The top view of the sequence depicted in figure 13 reveals that the symmetry plane for HP5 as it is advected downstream does not lie in the x_1–x_3 plane in contrast to that of HP4. They appear to disconnect in figure 13(*d*) after which HP4 develops into a vortex ring much like HP1 ($U^* = 4.5$, figure 10). Note that, in the supplementary movie file ('Fig 12.mp4'), an additional third hairpin vortex develops downstream of the sphere. This third vortex appears not to be associated with the actual shedding from the sphere but is rather a result of the instability of the legs of the second hairpin vortex as it develops into a vortex ring.

In the literature, few studies mention the shedding of four hairpins (or vortex rings) in the wake of a sphere. Based on dye visualisations, Horowitz & Williamson (2010) reported four vortex rings per oscillation cycle (so-called '4R' mode) in the wake of a light, freely rising sphere (zig-zag trajectory) that vibrates periodically. Interestingly, they showed that the generation of the '4R' mode only occurred when streamwise body vibrations were present, similar to the case in the present measurements (see figure 9).

In addition, time-resolved PIV measurements by van Hout *et al.* (2010) also reported the planar 'signatures' of four vortices shed per oscillation cycle for a tethered sphere at similar U^* and Re. However, they did not measure the 3-D vortex shedding structure which remained obscure.

An interesting question is, why are the 'double' hairpins generated for $U^* = 7.2 (Re = 850)$ and not for $U^* = 4.5 (Re = 532)$? The DNS study by Rajamuni *et al.* (2020) of a tethered neutrally buoyant sphere provides an indication. While keeping U^* constant, they reported that multiple loops were shed per oscillation cycle when Re was increased from 500 to 1200. Therefore, the answer must be related to the time scales associated with hairpin generation. Since in both cases, f_N is the same, the convective flow time scale, $t_f = D/U_\infty$, must play an important role. The ratio between the sphere's oscillation period, $T_s = 1/f_s \approx 1/f_N$ (lock-in), and t_f equals $T_s/t_f \approx (U_\infty f_N)/D \approx U^*$, i.e. T_s/t_f increases with U^* (or Re when keeping U^* constant as in Rajamuni *et al.* 2020). This indicates that, during one transverse 'sweep' of the sphere, more fluid passes it with increasing U^*. Therefore, as long as $f_s \approx f_N$ (i.e. in the lock-in region), one hairpin vortex will be generated for every $\Delta(T_s/t_f) \approx 3$, and additional hairpins may be generated providing T_s/t_f is sufficiently large, i.e. a multiple of ∼3, and 'lock-in' ($f_s \approx f_N$) occurs. We will show in § 3.2.1 that the hairpins shed at $U^* = 7.2$ provide more transverse forcing on the sphere resulting in a larger transverse amplitude response.

Similar to the cases of $U^* = 1.9$ and 3.2 (see § 3.1, figures 7 and 8), the instantaneous wake characteristics were analysed in transverse planes located at $x_1/D = 1.0$ and 3.0. Results depicting $(\theta^d, \rho^d/D)$ and $(\theta^v, \rho^v/D)$ are presented in the left and right columns of figure 14, respectively. In agreement with the alternately shedding of hairpin vortices having a symmetry plane perpendicular to gravity, values of θ^d mainly switch between 0° and 180° (figure 14*a*) indicating that $x^d_{i,c}/D$ (3.1) is located on the equatorial x_1–x_3 plane. The distance from the origin, ρ^d/D (figure 14*b*), fluctuates in the range $0.05 < \rho^d/D < 0.8$ and $0.05 < \rho^d/D < 0.5$ for $U^* = 4.5$ and 7.2, respectively. This shows that despite the increased transverse sphere oscillation amplitude at $U^* = 7.2$, maximum values of ρ^d/D at $x_1/D = 1.0$ are less than those for $U^* = 4.5$ at the same transverse plane as a result of the increased advection velocity of the hairpins for $U^* = 7.2$.

Values of θ^v concentrate in bands around ±90° (figure 14*c*), indicating that hairpin symmetry planes are perpendicular to gravity, in contrast to $U^* = 1.9$ and 3.2, where values of θ^v concentrate around 0° (figure 8*c*). The distance between the shed hairpin legs

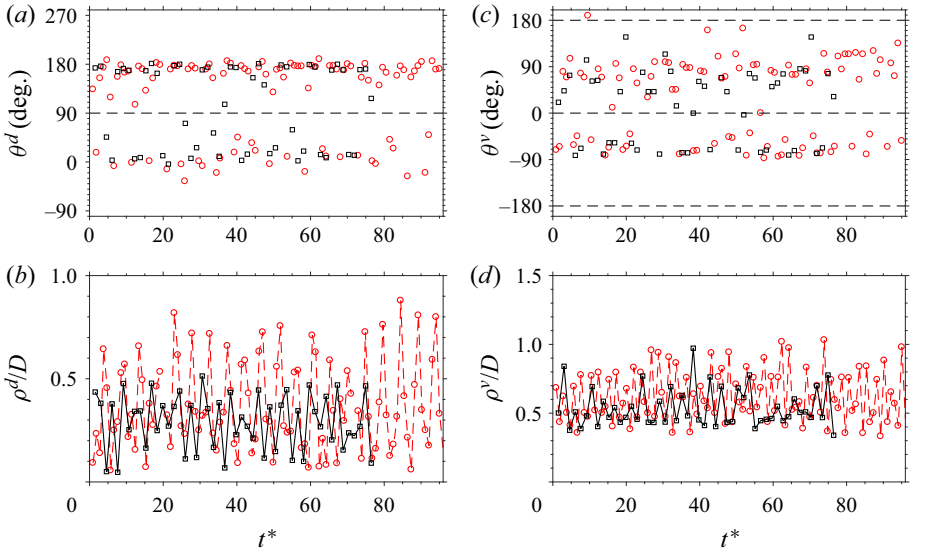

Figure 14. Instantaneous centroid positions of the velocity deficit (*a*,*b*) and the orientations and separation distances of the shed vortices (*c*,*d*) evaluated at a transverse plane located at $x_1/D = 1.0$ (*a*,*b*) and 3.0 (*c*,*d*); (*a*) θ^d, (*b*) ρ^d/D, (*c*) θ^v, (*d*) ρ^v/D. Here, $U^* = 4.5$ (○ – red), 7.2 (□).

fluctuates approximately in the range $0.4 < \rho^v/D < 0.8$ (figure 14*d*) for both U^* and will be used in the next section to determine the vortex force acting on the sphere. In § 4, we will further use this analysis to elucidate the chain of wake events accompanying the onset of VIV of a tethered sphere.

3.2.1. *Vortex force acting on the sphere*

For $U^* = 4.5$ and 7.2, the tethered sphere's amplitude response is within the 'lock-in' region and the shed vortices (Wu, Lu & Zhuang 2007) provide the transverse forcing that causes large amplitude, transverse oscillations. The force that causes the perturbation and pushes the sphere out of equilibrium is the so-called 'vortex force' (Lighthill 1986; Govardhan & Williamson 2005; Krakovich *et al.* 2013) which can be determined from the measured flow field in analogy with wing tip vortices. For example, the legs of hairpins HP1 and HP3 ($U^* = 4.5$, figure 10), expel fluid in the negative x_3-direction and, according to Newton's third law, a reaction force (the vortex force) acts on the sphere in the positive x_3-direction. Upon shedding HP1 (figure 10*a*), fluid forcing in the positive x_3-direction stops and gravity reverses the direction of the sphere's motion. This leads to the generation of HP2 (figure 10*b*) and fluid forcing on the sphere in the negative x_3-direction as this cycle repeats itself periodically.

The expression for the vortex force coefficient is given by Govardhan & Williamson (2005) and Krakovich *et al.* (2013) as

$$C_v = \frac{F_v}{\frac{1}{2}\rho_f U_\infty^2 A_s} = \frac{-U_v \Gamma \rho^v}{\frac{1}{2}U_\infty^2 A_s}, \tag{3.2}$$

where ρ_f is the fluid density, A_s denotes the cross-sectional area of the sphere, U_v denotes the hairpin's advection velocity and Γ is the circulation associated with the vortex legs. The normalised circulation was determined as the hairpin crossed the transverse plane at

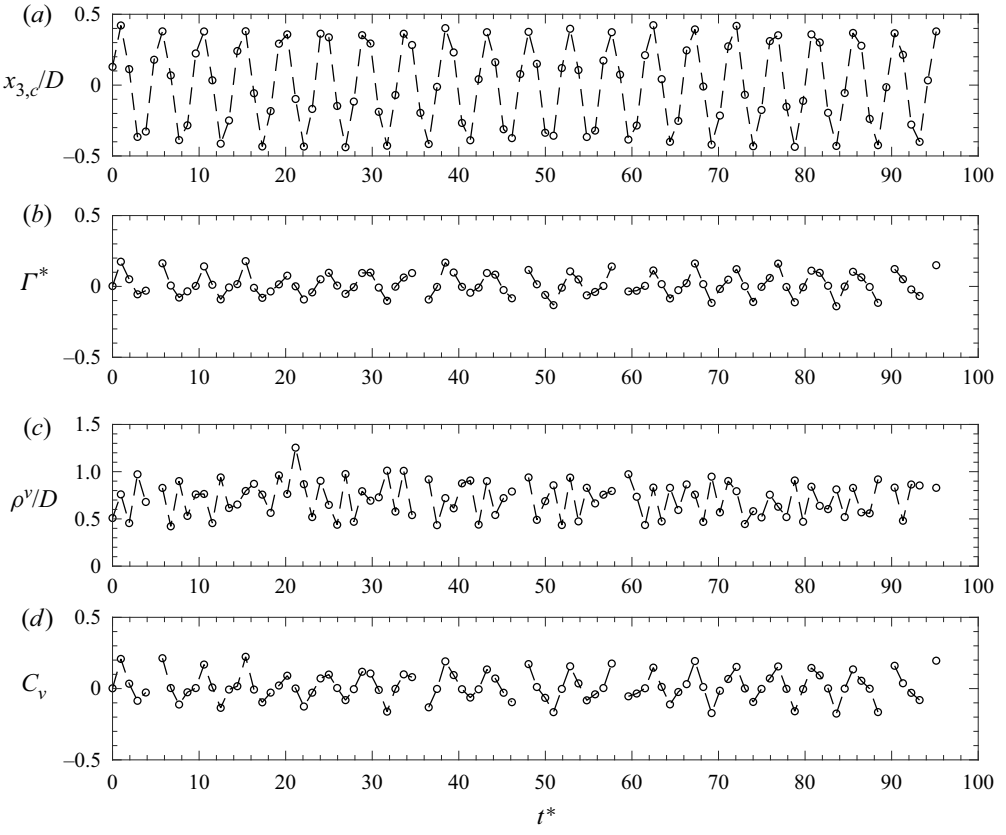

Figure 15. Analysis of the instantaneous vortex force coefficient as a function of t^* evaluated at a transverse plane located at $x_1/D = 2.0$, $U^* = 4.5$; (*a*) $x_{3,c}/D$, (*b*) Γ^*, (*c*) ρ^v/D and (*d*) C_v.

$x_1/D = 2.0$ (figure 7) by summing ω_1 over the area, A_v, associated with the vortex cores of the hairpin legs (see figure 7*b*)

$$\Gamma^* = \frac{1}{U_\infty D} \sum_{A_v} \omega_1 \, \mathrm{d}A_v. \tag{3.3}$$

Instantaneous values of $x_{3,c}/D$, Γ^*, ρ^v/D and C_v as a function of t^* are plotted in figures 15 and 16 for $U^* = 4.5$ and 7.2, respectively. The time series of $x_{3,c}/D$ in figures 15(*a*) and 16(*a*) show the periodic oscillations of the sphere for both U^* (see also figure 9). Values of ρ^v/D (figures 15*c* and 16*c*) do not drop below 0.5 and maxima reach $\rho^v/D \approx 1$ for $U^* = 4.5$ and are slightly lower for $U^* = 7.2$. Although the data are somewhat scattered as a result of the relatively low sampling frequency as well as difficulties in detecting clear vortex cores (especially for $U^* = 7.2$), the periodic nature of the determined C_v can be clearly observed in figures 15(*d*) and 16(*d*). Peak values of C_v are approximately 0.2 for $U^* = 4.5$ and reach about 0.3 for $U^* = 7.2$, in agreement with the increased transverse amplitude response at this U^*. Note that these values correspond well to those reported by Govardhan & Williamson (2005) and Krakovich *et al.* (2013). Further note that peak values of $|C_v|$ are asymmetric about zero as a result of the limited transverse extent of the VOI (see figures 11 and 13). A comparison between $x_{3,c}/D(t^*)$ (figures 15*a* and 16*a*) and $C_v(t^*)$ (figures 15*d* and 16*d*) reveals that the vortex phase, ϕ_v,

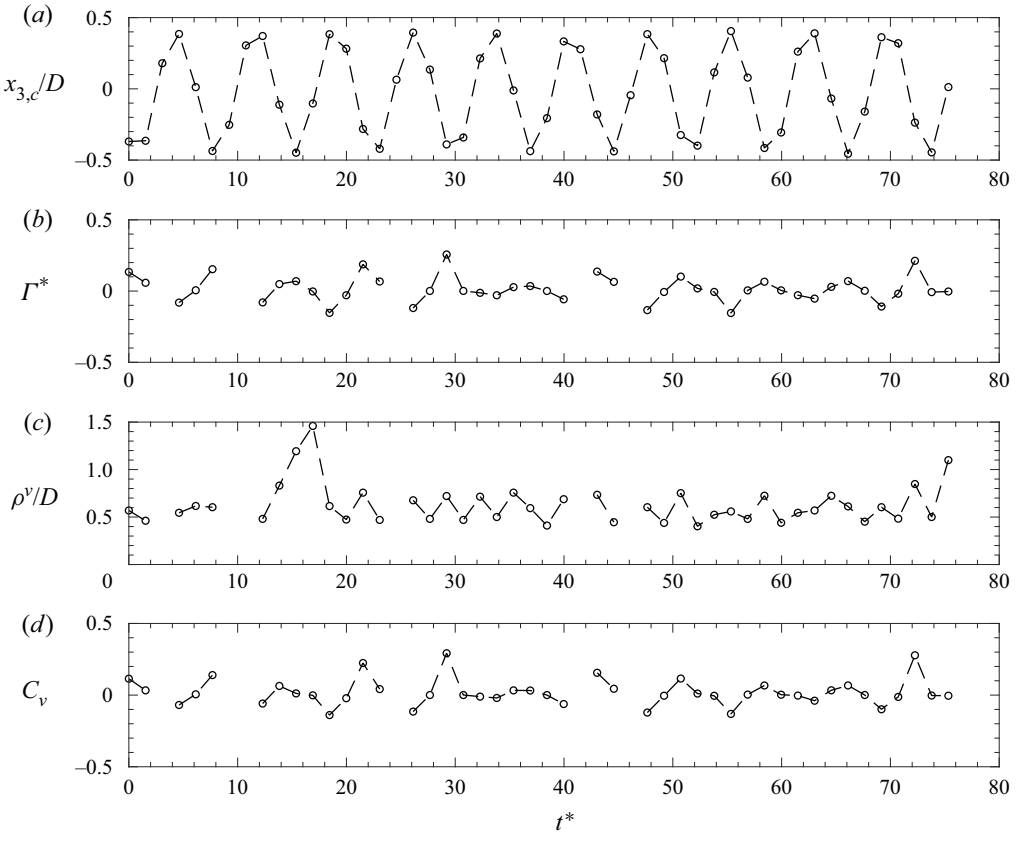

Figure 16. Analysis of the instantaneous vortex force coefficient as a function of t^* evaluated at a transverse plane located at $x_1/D = 2.0$, $U^* = 7.2$; (*a*) $x_{3,c}/D$, (*b*) Γ^*, (*c*) ρ^v/D and (*d*) C_v.

shifts from 0° for $U^* = 4.5$ to 180° for $U^* = 7.2$, i.e. in agreement with the transition from mode I to mode II for these U^* (Govardhan & Williamson 2005).

4. Sphere and wake dynamics: transient conditions

Up to this point, the vortex shedding in the wake of a tethered, heavy sphere has been characterised under steady, uniform upstream flow conditions and the results clearly indicated that crossing the Hopf bifurcation (onset of VIV) led to a 90° change in the orientation of the symmetry plane of the shed hairpin vortices. In order to elucidate the changes in the flow field accompanying the onset of VIV, the tethered sphere was exposed to a time-dependent uniform upstream velocity, $U_\infty(t)$, by stepwise increasing U^* from 2.2 ($t^* = 0$) to 4.5 ($t^* = 725$) (see figure 17*a*). Simultaneously, the sphere's centroid position was tracked and its transverse and streamwise positions (relative to the sphere at rest) are depicted in figures 17(*b*) and 17(*c*), respectively. The vertical dash lines in figure 17 indicate the time ($t^* = 718$) at which $U^* = 4.5$ was reached and kept constant. Due to the drag force, the sphere is increasingly displaced in the streamwise direction (figure 17*c*) as U^* is increased to 4.5. For $t^* > 1100 (U^* = 4.5)$, fluctuations of $x_{1,c}/D$ about its mean value compare well with those obtained under steady upstream flow conditions (see figure 9*d*). In the transverse direction, the sphere only started to oscillate shortly after reaching $U^* = 4.5$ at $t^* \approx 800$ (figure 17*b*). Its maximum transverse centroid position,

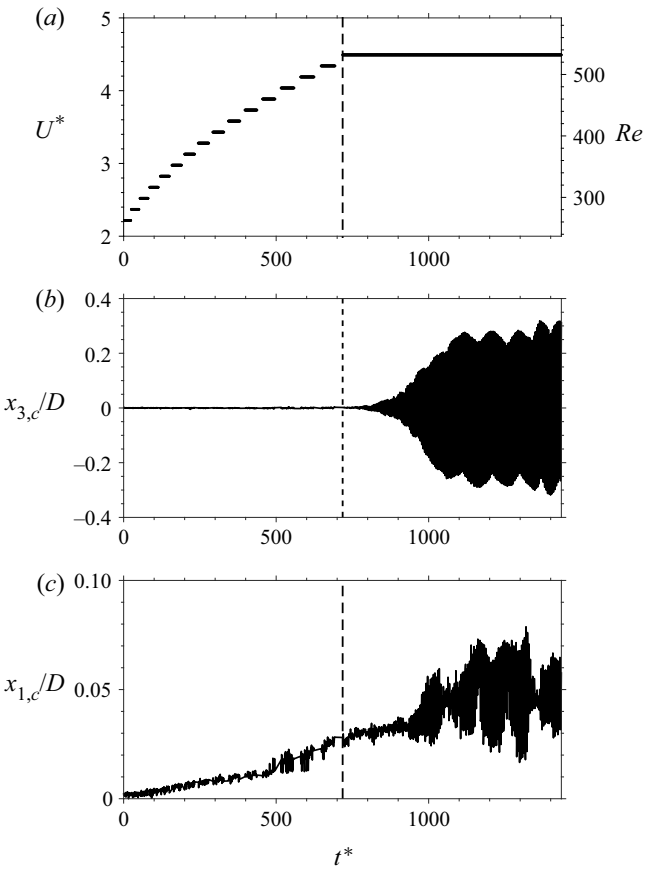

Figure 17. Transient upstream flow conditions: (*a*) stepwise increase in U^* (and Re) as a function of t^*, and the simultaneously measured sphere centroid positions in the (*b*) transverse and (*c*) streamwise directions. Dashed line indicates the time ($t^* = 718$) at which $U^* = 4.5$ is reached.

$(x_{3,c}/D)_{max}$, increased at first slowly up to $t^* \approx 900$, and subsequently at an increasing rate between $900 < t^* < 1100$. Beyond $t^* \approx 1100$, $(x_3/D)_{max} \approx 0.3$, i.e. comparable to that attained for the steady state case at the same U^* (figure 3). Note that the observed fluctuations of $(x_{3,c}/D)_{max}$ are the result of the limited sampling frequency. Further note that the power spectrum based on $x_{3,c}/D(t^*)$ for $t^* > 1100$ (not shown here), was similar as the one obtained under steady upstream flow conditions (see figure 9*c*) with $f_s/f_N = 0.94$.

Four snapshots of the vortex structure in the wake of the tethered sphere at $U^* = 2.8 (t^* = 134.2)$, 3.9 ($t^* = 465.9$), 4.2 ($t^* = 592.0$) and 4.5 ($t^* = 1419.7$) are depicted in figure 18. The snapshots at the two lowest U^* (figure 18*a*,*b*) clearly show that the vortex structure resembles the one observed under steady upstream flow conditions at similar U^*. For example, the pair of counter-rotating longitudinal vortices in figure 18(*a*) strongly resembles those observed in figure 5(*c*), and the uplifted hairpin vortex and the legs of the induced vortices depicted in figure 18(*b*) are almost identical to those in figure 6(*d*). At $U^* = 4.2$ (figure 18*c*), the symmetry plane of the shed hairpins becomes unstable, as illustrated by the appearance of 'twisted' hairpins shed at this instant. For $t^* = 1419.7 (U^* = 4.5)$, alternately shed, single hairpin vortices with their symmetry planes perpendicular to gravity are observed (figure 18*d*) similar to those depicted in figure 10 under steady upstream flow conditions. However, the hairpins observed at this

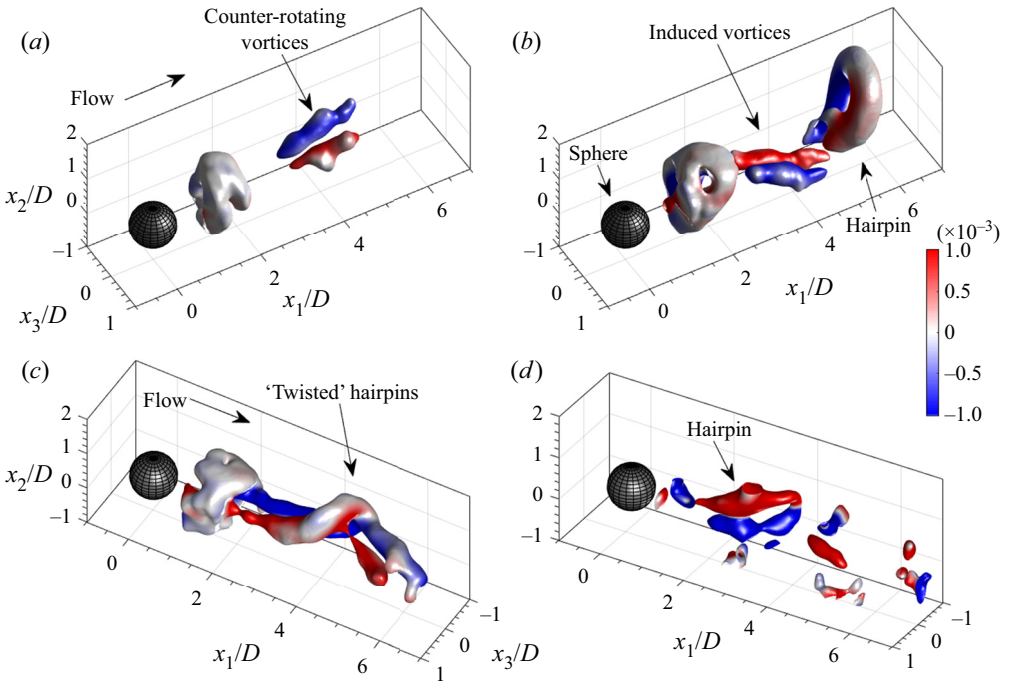

Figure 18. Example snapshots of the vortex shedding structure in the wake of the tethered sphere under transient upstream flow conditions visualised by Q-criterion iso-surfaces overlaid by ω_1^*; (U^*, t^*) = (*a*) (2.8,134.2), (*b*) (3.9,465.9), (*c*) (4.2,592.0) and (*d*) (4.5,1419.7).

stage were never as pronounced as those observed under steady upstream flow conditions (figure 10), and in most cases only the counter-rotating legs were observed.

In order to gain more insight into the wake dynamics accompanying the onset of VIV of the tethered sphere, the transient data set was analysed using the two approaches presented in §§ 3.1 and 3.2 (see figures 8 and 14). The centroid positions of the velocity deficit and the relative positions of the hairpin legs were analysed in transverse planes located at $x_1/D = 1.0$ (velocity deficit), and $x_1/D = 3.0$ (hairpin legs). Instantaneous values of θ^d and ρ^d/D are depicted in figures 19(*a*) and 19(*b*), respectively, as a function of both U^* and t^*, superimposed on the transverse response 'envelope' of the sphere (depicted as a light blue, semi-transparent surface). As expected for an uplifted wake with a symmetry plane aligned with gravity, up to $U^* \approx 4 (Re < 470, t^* < 600)$, θ^d remains nearly constant at 90° (figure 19*a*), while ρ^d/D slightly decreases from $\rho^d/D \approx 0.3$ to 0.26 between $t^* = 0$ and 600, respectively.

Beyond $U^* \approx 4 (t^* \approx 600)$, values of θ^d and ρ^d/D drastically change. Between $U^* = 4$ and 4.5 while the sphere remains almost stationary (figure 17*b*,*c*), ρ^d/D quickly reduces to almost zero (figure 19*b*). At the same time, θ^d shows a preference for angles smaller than 90°. The strong reduction of ρ^d/D is due to the loss of the preferred orientation of the symmetry plane of the shed vortices as illustrated in figure 18(*c*). Consequently, the repeating self-induced upward inclination of the shed hairpins is lost, and $x^d_{i,c}/D$ becomes centred at the origin. Between $t^* = 718 (U^* = 4.5)$ and the onset of transverse sphere motion ($t^* \approx 800$, see figure 17*a*), ρ^d/D remains close to zero (figure 19*b*) while θ^d 'samples' all possible angles (figure 19*a*). This indicates that, due to system inertia, it takes time before a preferred orientation and lock-in is attained. As the sphere starts

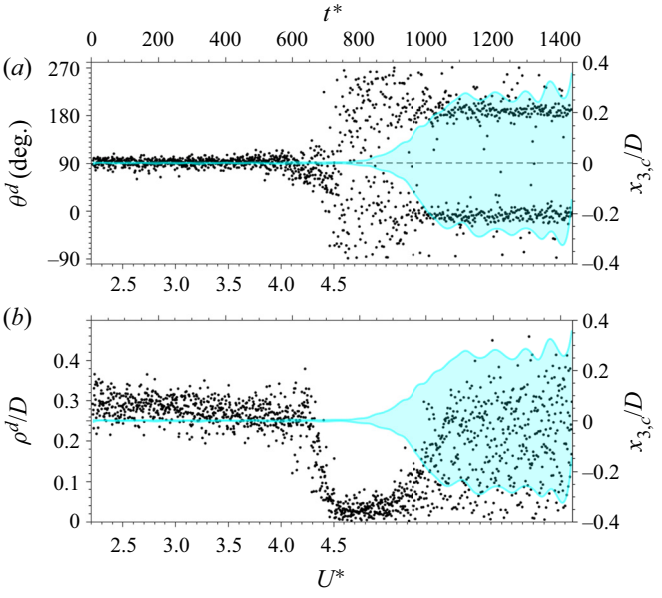

Figure 19. Instantaneous values of (*a*) θ^d, and (*b*) ρ^d/D as a function of U^* and t^* overlaid on the transverse sphere response (light blue envelope, secondary y-axis).

to move and transitions to its maximum transverse response ($800 < t^* < 900$), ρ^d/D remains close to zero while θ^d remains scattered. However, in the range $900 < t^* < 1100$, as the transverse sphere response quickly grows (figure 17*b*), values of θ^d converge to two branches having mean values of $\theta^d \approx 0^\circ$ and 180°, while values of ρ^d/D fluctuate between $0 < \rho^d/D < 0.4$. Beyond $t^* = 1100$, as the shed vortices in the wake of the tethered sphere (figure 18*d*) increasingly resemble those observed under steady upstream flow conditions (figure 10), the two θ^d branches become highly pronounced and correspond to the wake 'flipping' sides as the hairpin vortices are periodically shed from alternating sides (see figures 10 and 12).

In conclusion, our results show that, prior to the onset of VIV between $4 < U^* < 4.5$, the pending transition manifests itself in the wake by (i) a strong decrease of ρ^d/D to zero and by (ii) initially small deviations from $\theta^d = 90^\circ$ (symmetry breaking). After reaching $U^* = 4.5$, the wake is initially disorganised without any preferred orientation of the shed vortices, i.e. θ^d samples all possible values while ρ^d/D remains close to zero. As transverse sphere movement starts, the wake is reorganised and values of θ^d converge in two branches, $\theta^d = 180^\circ$ and 0°, in agreement with alternately shed hairpin vortices having a horizontal plane of symmetry (figures 10 and 12).

The structure and organisation of the shed vortices is further analysed by the instantaneous values of θ^v and ρ^v/D that are depicted in figures 20(*a*) and 20(*b*), respectively. As expected, up to $U^* = 3$, $\theta^v \approx 0^\circ$ (figure 20*a*), while $\rho^v/D \approx 0.5$ up to $U^* \approx 2.8$ (figure 20*b*). In the range $3 \leq U^* \leq 3.6$, two additional branches appear at $\theta^v = \pm 180^\circ$ (figure 20*a*). These are linked to the induced vortices (figure 6*d–f*) whose counter-rotating longitudinal legs are of opposite sign compared with those of the primary hairpin vortices (see figure 18*b*). Therefore, as a result of measuring θ^v in the direction from negative to positive vorticity, θ^v flips from 0° to $\pm 180^\circ$ when their symmetry plane is almost perpendicular to gravity. While induced vortices have been identified numerically

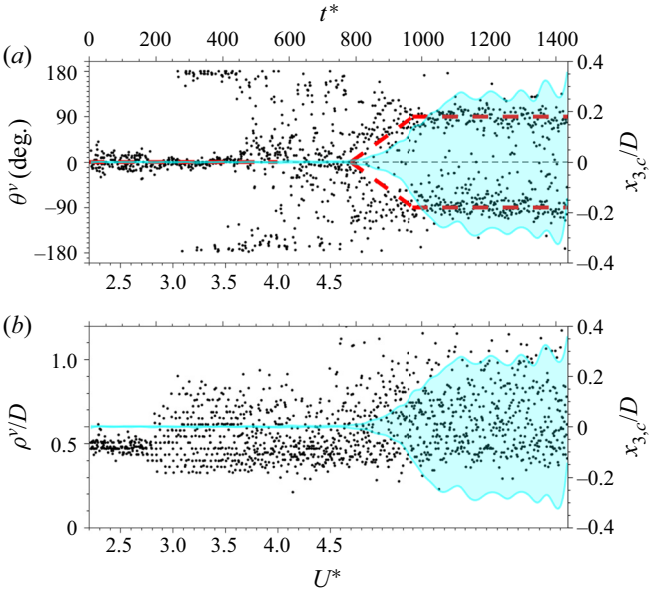

Figure 20. Instantaneous values of (*a*) θ^v, and (*b*) ρ^v/D as a function of U^* and t^* overlaid on the transverse sphere response (light blue envelope, secondary *y*-axis). Dash red lines in (*a*) illustrate trends.

(Johnson & Patel 1999) as well as experimentally (Eshbal *et al.* 2019*b*) for fixed spheres, these results show that they first appear at $Re \approx 360 (U^* \approx 3)$ for a tethered sphere. Note that, at the same time, ρ^v/D fluctuates between $0.3 < \rho^v/D < 0.9$ (figure 20*c*).

Beyond $U^* = 3.6 (t^* \approx 343, Re \approx 430)$, values of θ^v become scattered and are in the range $-180^\circ \leq \theta^v < 180^\circ$ (figure 20*b*), while those of ρ^v/D remain scattered with a slightly larger likelihood of being close to 0.5. This region extends to $t^* \approx 800$ and can be considered the region in which the symmetry plane orientation becomes unstable while transverse sphere oscillations are absent (figure 17*b*). The Reynolds number, $Re \approx 430$ (at $t^* = 343$, $U^* = 3.6$), for the onset of planar symmetry loss is somewhat higher than $Re = 375$ reported by Chrust *et al.* (2013), but similar to that reported by Sakamoto & Haniu (1990) ($Re = 420$) for a fixed sphere. Just after reaching $U^* = 4.5$, the sphere starts to oscillate in the transverse direction ($t^* \approx 800$, figure 17*b*) and the transition to a symmetry plane perpendicular to gravity (figure 10) is manifested by the convergence of the values of θ_v into two branches, $\theta_v = \pm 90^\circ$ for $U^* > 4.5, t^* > 800$ (trends are highlighted by dash red lines in figure 20*a*). Note that this is similar to what was obtained under steady conditions at $U^* = 4.5$ (figure 14*c*).

5. Summary and discussion

We have presented a detailed analysis of the changes in the vortex shedding patterns accompanying the onset of VIV for a heavy, tethered sphere. The analysis was based on the results of simultaneous 3-D flow field measurements (tomo-PIV) and sphere position tracking. The 3-D flow field in the wake of the tethered sphere was measured under both steady and transient upstream flow conditions. The former were performed at $U^* = 1.9$, 3.2, 4.5 and 7.2 corresponding to $Re = 230$, 383, 532 and 850, respectively, while transient upstream flow conditions were imposed by stepwise increasing U^* within the range, $2.2 < U^* < 4.5 (263 < Re < 532)$. Note that U^* and Re are not independent, and while

both are proportional to U_∞, Re and U^* are proportional and inversely proportional to D, respectively. Therefore, increasing Re while keeping U^* in the 'lock-in' regime would require to increase the sphere diameter (for given fluid kinematic viscosity and tether length). The present range of Re was chosen such that distinct, well-organised large-scale vortex shedding was obtained that could be well resolved (both spatially and temporally) by the employed tomo-PIV method.

The combination of measurements under steady and transient upstream flow conditions allowed for (i) a detailed comparison between the observed vortex shedding patterns, and (ii) us to elucidate the chain of wake events accompanying the onset of VIV. The latter was quantified by the instantaneous centroid positions of the velocity deficit and the instantaneous symmetry plane orientations of the shed longitudinal vortices in the near wake of the sphere. Our results showed that sphere VIV are initiated through a complex chain of events first manifested by 'lock-in' of streamwise sphere oscillations due to the appearance of induced vortices at $U^* \approx 3 (Re \approx 360)$. As the shed hairpins become unstable with increasing U^*, their small transverse perturbations are transferred to the tethered sphere, which leads to amplification of its transverse oscillation and greater instability of the shed hairpins. With the tether constraining the sphere's motion, this process mutually reinforces transverse oscillation and reorganises the flow field such that the shed hairpins' symmetry planes are flipped by 90° and their forcing sustains VIV.

Several stages were identified in the onset of VIV. First, at low $U^* (< 3)$, shed primary hairpin orientations were stable exhibiting a symmetry plane oriented in the streamwise direction parallel with the tether. The wake was consistently lifted upwards due to self-induced motion ($\rho^d/D \approx 0.3$, $\theta^d \approx 90°$). In the second stage ($3 < U^* < 4.2$), induced vortices appeared that led to lock-in of the sphere's streamwise oscillations, prior to lock-in in the transverse direction. In the third stage, for transient upstream flow conditions in the range $4.2 < U^* < 4.5$, impending sphere oscillations were manifested by a rapid decrease of ρ^d/D to almost zero due to loss of the hairpin's preferred orientation. At this stage, the wake's velocity deficit became centred in the downstream direction (along $x_2 = x_3 = 0$). After reaching $U^* = 4.5$ (fourth stage, transient conditions), transverse sphere oscillations only started after a delay ($\Delta t^* \approx 100$) due to system inertia. During this stage, vortex shedding was unorganised, lacking any preferred orientation. However, the interaction between the shed vortices and the tethered sphere's constrained ability to move, led to concurrent amplification of the sphere's transverse oscillation amplitude and simultaneous reorganisation of the shed hairpin orientations into two branches ($\theta^v = \pm 90°$) reaching the same state as for $U^* = 4.5$ under steady upstream flow conditions.

After crossing the onset of VIV, the tethered sphere exhibited streamwise and transverse periodic oscillations at a frequency close to f_N within the lock-in region at $U^* = 4.5$ (mode I) and 7.2 (mode II). Shedding was characterised by a sequence of alternately shed hairpin vortices having a symmetry plane perpendicular to gravity with the transverse r.m.s. oscillation amplitude for $U^* = 7.2$ exceeding that for $U^* = 4.5$. The elevated transverse r.m.s. oscillation amplitude at $U^* = 7.2$ was accompanied by shedding of pairs of double hairpin vortices per oscillation cycle. In contrast, at $U^* = 4.5$ only pairs of single hairpins were shed per oscillation cycle. Calculation of the instantaneous vortex force exerted on the sphere by the fluid showed that maximum magnitudes of the vortex force exerted on the sphere at $U^* = 7.2$ exceeded those at $U^* = 4.5$ in accordance with the increased transverse oscillation amplitude. We associated the generation of multiple single-sided hairpin vortices per oscillation cycle with the ratio $T_f/t_s \approx U^*$ (as long as $f_s \approx f_N$), i.e. multiple single-sided hairpins may be generated during one transverse sweep

of the sphere providing U^* is large enough (multiple of approximately 3) and within the lock-in region. Note that, for a light sphere ($m^* < 1$), the lock-in region widens (Govardhan & Williamson 2005) and, according to the suggested mechanism, multiple (three or more) single-sided hairpins may be shed during one oscillation cycle with increasing U^*.

It should be noted that the basic mechanism for the onset of VIV lies in boundary layer and shear layer instabilities that develop close to the sphere's surface (van Hout, Katz & Greenblatt 2013*a*; van Hout *et al.* 2013*b*), and are difficult to resolve experimentally even at the relatively low Reynolds number range that was chosen. However, the present results show that the signature of these boundary layer instabilities can be detected in transverse planes, downstream of the sphere. A higher Reynolds number range can be explored by choosing a larger sphere (while keeping m^* the same). Although we expect that similar physical mechanisms also act at higher Reynolds numbers (based on similar vortex shedding topology and transverse sphere response, see Govardhan & Williamson 2005, Rajamuni *et al.* 2018, 2020), vortex shedding patterns may become less organised and more fragmented, possibly affecting some of the present findings regarding the change of the velocity deficit centroid positions and the relative position of shed longitudinal vortices. This is outside the scope of the present investigation and will be investigated in future studies.

Furthermore, while the present results have provided much insight into the sequence of events leading to VIV of a tethered sphere, time scales associated with the changing upstream flow field and associated response of the tethered sphere (dependence of m^*) were outside the scope of the present investigation. However, they are clearly of interest in practical applications and will be pursued in future research.

Supplementary movies. Supplementary movies are available at https://doi.org/10.1017/jfm.2022.428.

Funding. This research was supported by the Israel Science Foundation under grant no. 1596/14.

Declaration of interest. The authors report no conflict of interest.

Author ORCIDs.
R. van Hout https://orcid.org/0000-0002-4042-7936.

References

Achenbach, E. 1974 Vortex shedding from spheres. *J. Fluid Mech.* **62** (02), 209–221.
Adrian, R.J. & Westerweel, J. 2011 *Particle Image Velocimetry*. Cambridge University Press.
Bearman, P.W. 1984 Vortex shedding from oscillating bluff bodies. *Annu. Rev. Fluid Mech.* **16**, 195–222.
Behara, S., Borazjani, I. & Sotiropoulos, F. 2011 Vortex-induced vibrations of an elastically mounted sphere with three degrees of freedom at $Re = 300$: hysteresis and vortex shedding modes. *J. Fluid Mech.* **686**, 426–450.
Behara, S. & Sotiropoulos, F. 2016 Vortex-induced vibrations of an elastically mounted sphere: the effects of Reynolds number and reduced velocity. *J. Fluids Struct.* **66**, 54–68.
Bernitsas, M.M., Raghavan, K., Ben-Simon, Y. & Garcia, E.M. 2008 Vivace (vortex induced vibration aquatic clean energy): a new concept in generation of clean and renewable energy from fluid flow. *Trans. ASME J. Offshore Mech. Arctic Engng* **130** (4), 041101.
Blevins, R.D. 1977 *Flow-Induced Vibration*. Van Nostrand Reinhold Co.
Chrust, M., Goujon-Durand, S. & Wesfreid, J.E. 2013 Loss of a fixed plane of symmetry in the wake of a sphere. *J. Fluids Struct.* **41**, 51–56.
David, T., Eshbal, L., Rinsky, V. & van Hout, R. 2020 Flow measurements in the near wake of a smooth sphere and one mimicking a pine cone. *Phys. Rev. Fluids* **5** (7), 074301.
Elsinga, G.E., Adrian, R.J., van Oudheusden, B.W. & Scarano, F. 2010 Three-dimensional vortex organization in a high-Reynolds-number supersonic turbulent boundary layer. *J. Fluid Mech.* **644**, 35–60.
Eshbal, L., Kovalev, D., Rinsky, V., Greenblatt, D. & van Hout, R. 2019*a* Tomo-piv measurements in the wake of a tethered sphere undergoing VIV. *J. Fluids Struct.* **89**, 132–141.

ESHBAL, L., KRAKOVICH, A. & VAN HOUT, R. 2012 Time resolved measurements of vortex-induced vibrations of a positively buoyant tethered sphere in uniform water flow. *J. Fluids Struct.* **35**, 185–199.

ESHBAL, L., RINSKY, V., DAVID, T., GREENBLATT, D. & VAN HOUT, R. 2019*b* Measurement of vortex shedding in the wake of a sphere at $Re = 465$. *J. Fluid Mech.* **870**, 290–315.

GOVARDHAN, R.N. & WILLIAMSON, C.H.K. 1997 Vortex-induced motions of a tethered sphere. *J. Wind Engng Ind. Aerodyn.* **69**, 375–385.

GOVARDHAN, R.N. & WILLIAMSON, C.H.K. 2005 Vortex-induced vibrations of a sphere. *J. Fluid Mech.* **531**, 11–47.

GRANDEMANGE, M., CADOT, O. & GOHLKE, M. 2012 Reflectional symmetry breaking of the separated flow over three-dimensional bluff bodies. *Phys. Rev.* E **86** (3), 035302.

GRANDEMANGE, M., GOHLKE, M. & CADOT, O. 2014 Statistical axisymmetry of the turbulent sphere wake. *Exp. Fluids* **55** (11), 1838.

HOROWITZ, M. & WILLIAMSON, C.H.K. 2010 The effect of Reynolds number on the dynamics and wakes of freely rising and falling spheres. *J. Fluid Mech.* **651**, 251–294.

VAN HOUT, R., EISMA, J., ELSINGA, G.E. & WESTERWEEL, J. 2018 Experimental study of the flow in the wake of a stationary sphere immersed in a turbulent boundary layer. *Phys. Rev. Fluids* **3** (2), 024601.

VAN HOUT, R., KATZ, A. & GREENBLATT, D. 2013*a* Acoustic control of vortex-induced vibrations of a tethered sphere. *AIAA J.* **51** (3), 754–757.

VAN HOUT, R., KATZ, A. & GREENBLATT, D. 2013*b* Time-resolved particle image velocimetry measurements of vortex and shear layer dynamics in the near wake of a tethered sphere. *Phys. Fluids* **25** (7), 77–102.

VAN HOUT, R., KRAKOVICH, A. & GOTTLIEB, O. 2010 Time resolved measurements of vortex-induced vibrations of a tethered sphere in uniform flow. *Phys. Fluids* **22** (8), 087101.

HUNT, J.C.R., WRAY, A.A. & MOIN, P. 1988 Eddies, streams, and convergence zones in turbulent flows. In *Proceedings of the 1988 Summer Program of the Center for Turbulence Research*, pp. 193–208. NASA Ames/Stanford University.

JAUVTIS, N., GOVARDHAN, R. & WILLIAMSON, C.H.K. 2001 Multiple modes of vortex-induced vibration of a sphere. *J. Fluids Struct.* **15** (3–4), 555–563.

JOHNSON, T.A. & PATEL, V.C. 1999 Flow past a sphere up to a Reynolds number of 300. *J. Fluid Mech.* **378**, 19–70.

KRAKOVICH, A., ESHBAL, L. & VAN HOUT, R. 2013 Vortex dynamics and associated fluid forcing in the near wake of a light and heavy tethered sphere in uniform flow. *Exp. Fluids* **54** (11), 1615.

LEE, H., HOURIGAN, K. & THOMPSON, M.C. 2013 Vortex-induced vibration of a neutrally buoyant tethered sphere. *J. Fluid Mech.* **719**, 97–128.

LEWEKE, T., LE DIZES, S. & WILLIAMSON, C.H.K. 2016 Dynamics and instabilities of vortex pairs. *Annu. Rev. Fluid Mech.* **48**, 507–541.

LEWEKE, T., PROVANSAL, M., ORMIERES, D. & LEBESCOND, R. 1999 Vortex dynamics in the wake of a sphere. *Phys. Fluids* **11** (9), S12.

LIGHTHILL, J. 1986 Fundamentals concerning wave loading on offshore structures. *J. Fluid Mech.* **173**, 667–681.

MAGARVEY, R.H. & BISHOP, R.L. 1961 Wakes in liquid-liquid systems. *Phys. Fluids* **4** (7), 800–805.

MAGARVEY, R.H. & MACLATCHY, C.S. 1965 Vortices in sphere wakes. *Can. J. Phys.* **43** (9), 1649–1656.

MITTAL, R. 1999 Planar symmetry in the unsteady wake of a sphere. *AIAA J.* **37** (3), 388–390.

MÖLLER, W. 1938 Experimentelle Untersuchungen zur Hydrodynamik der Kugel. *Phys. Z.* **2**, 57–80.

NAUDASCHER, E. & ROCKWELL, D. 2012 *Flow-Induced Vibrations: An Engineering Guide*. p. 767. Dover Publications.

ORMIÈRES, D. & PROVANSAL, M. 1999 Transition to turbulence in the wake of a sphere. *Phys. Rev. Lett.* **83** (1), 80–83.

RAJAMUNI, M.M., THOMPSON, M.C. & HOURIGAN, K. 2018 Transverse flow-induced vibrations of a sphere. *J. Fluid Mech.* **837**, 931–966.

RAJAMUNI, M.M., THOMPSON, M.C. & HOURIGAN, K. 2020 Vortex dynamics and vibration modes of a tethered sphere. *J. Fluid Mech.* **885**, A10.

SAKAMOTO, H. & HANIU, H. 1990 A study on vortex shedding from spheres in a uniform flow. *J. Fluids Engng* **112**, 386–392.

SAREEN, A., ZHAO, J., SHERIDAN, J., HOURIGAN, K. & THOMPSON, M.C. 2018 The effect of imposed rotary oscillation on the flow-induced vibration of a sphere. *J. Fluid Mech.* **855**, 703–735.

SARPKAYA, T. 2004 A critical review of the intrinsic nature of vortex-induced vibrations. *J. Fluids Struct.* **19** (4), 389–447.

SZALTYS, P., CHRUST, M., PRZADKA, A., GOUJON-DURAND, S., TUCKERMAN, L.S. & WESFREID, J.E. 2011 Nonlinear evolution of instabilities behind spheres and disks. *J. Fluids Struct.* **27** (5-6), 743–747.

TOMBOULIDES, A.G. & ORSZAG, S.A. 2000 Numerical investigation of transitional and weak turbulent flow past a sphere. *J. Fluid Mech.* **416**, 45–73.

WESTERWEEL, J. & SCARANO, F. 2005 Universal outlier detection for PIV data. *Exp. Fluids* **39** (6), 1096–1100.

WILLIAMSON, C.H.K. & GOVARDHAN, R. 2004 Vortex-induced vibrations. *Annu. Rev. Fluid Mech.* **36**, 413–455.

WU, J.-Z., LU, X.-Y. & ZHUANG, L.-X. 2007 Integral force acting on a body due to local flow structures. *J. Fluid Mech.* **576**, 265–286.